JGR Atmospheres

RESEARCH ARTICLE
10.1029/2021JD035112

Predicting Frigid Mixed-Phase Clouds for Pristine Coastal Antarctica

Keith M. Hines[1], David H. Bromwich[1,2], Israel Silber[3], Lynn M. Russell[4], and Lesheng Bai[1]

[1]Polar Meteorology Group, Byrd Polar & Climate Research Center, The Ohio State University, Columbus, OH, USA, [2]Department of Geography, Atmospheric Sciences Program, The Ohio State University, Columbus, OH, USA, [3]Department of Meteorology and Atmospheric Sciences, The Pennsylvania State University, University Park, PA, USA, [4]Scripps Institution of Oceanography, University of California San Diego, La Jolla, CA, USA

Abstract Supercooled water is common in the clouds near coastal Antarctica and occasionally occurs at temperatures at or below −30°C. Yet the ice physics in most regional and global numerical models will glaciate out these clouds. This presents a challenge for the simulation of highly supercooled clouds that were observed at McMurdo, Antarctica during the Atmospheric Radiation Measurement (ARM) West Antarctic Radiation Experiment (AWARE) project during 2015–2017. The polar optimized version of the Weather Research and Forecasting model (Polar WRF) with the recently developed two-moment P3 microphysics scheme was used to simulate observed supercooled liquid water cases during March and November 2016. Nudging of the simulations to observed rawinsonde profiles and Antarctic automatic weather station observations provided increased realism and much greater cloud water amounts. Sensitivity tests that adjust the ice physics for extremely low ice nucleating particle (INP) concentrations decrease cloud ice and increases the cloud liquid water closer to observed amounts. In these tests, a liquid layer near cloud top is simulated, in agreement with observations. Accurate representation of INP concentrations appears to be critical for the simulation of coastal Antarctic clouds.

Plain Language Summary Liquid water is common in the clouds observed at McMurdo Station located on Ross Island, Antarctica. The liquid water occurs even when the temperature is well below freezing and ice might be expected from the common physics of clouds. The pristine atmosphere there has very few particles that are favorable for the formation of cloud ice. Models with cloud physics set for more populated regions of Earth therefore have difficulty simulating these cold liquid clouds. When we adjust our regional model Polar WRF for the pristine conditions, it improves the simulation of the liquid clouds. Also, our simulations can underrepresent the amount of water substance in vapor form in the coastal Antarctic atmosphere. This error appears to arise from the dry external forcing source we use for the regional simulations. When we adjust the simulations by gradually nudging toward balloon-based observations at McMurdo and other regional observations the amount of vapor increases toward observed values. This has the beneficial result of improving the simulation of clouds. We believe that atmospheric models need to better represent the particulates in the atmosphere to improve the cloud simulations near Antarctica and elsewhere.

Key Points:

- Data assimilation increases the modeled water vapor closer to observed amounts and improves Antarctic clouds in mesoscale simulations
- Adding realistic ice nucleating particle (INP) concentrations in models improves simulated clouds in better agreement with observations
- Highly supercooled liquid water extending to cloud tops observed at McMurdo can properly be simulated by specifying sparse amounts of INP

Supporting Information:

Supporting Information may be found in the online version of this article.

Correspondence to:

K. M. Hines,
hines.9l@osu.edu

Citation:

Hines, K. M., Bromwich, D. H., Silber, I., Russell, L. M., & Bai, L. (2021). Predicting frigid mixed-phase clouds for pristine coastal Antarctica. *Journal of Geophysical Research: Atmospheres*, *126*, e2021JD035112. https://doi.org/10.1029/2021JD035112

Received 30 APR 2021
Accepted 9 NOV 2021

Author Contributions:

Conceptualization: David H. Bromwich
Data curation: Israel Silber, Lynn M. Russell, Lesheng Bai
Formal analysis: Keith M. Hines, Israel Silber
Funding acquisition: David H. Bromwich
Investigation: Keith M. Hines
Methodology: Keith M. Hines
Project Administration: David H. Bromwich, Lynn M. Russell
Resources: David H. Bromwich, Israel Silber, Lynn M. Russell, Lesheng Bai
Software: Lesheng Bai
Supervision: David H. Bromwich
Writing – original draft: Keith M. Hines
Writing – review & editing: David H. Bromwich, Israel Silber, Lynn M. Russell

1. Introduction

Supercooled liquid water is common in polar clouds and strongly impacts the radiative balance in both the Arctic and Antarctic regions (Intrieri et al., 2002; Listowski et al., 2019; McFarquhar et al., 2021; Morrison et al., 2012; Shupe et al., 2015; Silber, Verlinde, Cadeddu, et al., 2019). In some cases, supercooled liquid water may occur in narrow layers near the top of clouds where cloud top cooling and turbulent vertical motions promote condensation (Korolev et al., 2017; Morrison et al., 2012; Vignon et al., 2021). Liquid water has stronger radiative impact on longwave and shortwave fluxes than cloud ice, so the presence of liquid enhances the climate impact of polar clouds (Grosvenor et al., 2012; McCoy et al., 2015; Shupe & Intrieri, 2004). Accordingly, liquid water can enhance cloud-induced surface warming over Antarctica (Hines et al., 2019; Nicolas et al., 2017; Scott et al., 2017, 2019). We need to accurately represent the cloud radiative effect in the Antarctic region for proper simulations of the 21st Century climate, which is closely linked with ice melt and global sea level rise (Bromwich et al., 2012, 2013; Hyder et al., 2018; Rignot, 2008; Steig et al., 2009).

Unfortunately, much is still unknown about Antarctic and Southern Ocean clouds, largely due to the limited regional observations (Bromwich et al., 2012; Lachlan-Cope et al., 2016; McFarquhar et al., 2021; Scott & Lubin, 2016). Observational studies show high southern latitude clouds have different characteristics than the more frequently studied Arctic clouds, perhaps in part due to the different aerosol seasonal cycles in the much more pristine Southern Hemisphere than in the Northern Hemisphere (Bromwich et al., 2012; Grosvenor et al., 2012; Hogan, 1986; Lubin et al., 2020; O'Shea et al., 2017). Moreover, climate modeling studies show large uncertainty in high southern latitudes, which limits our ability to understand and predict 21st Century climate change (e.g., Hyder et al., 2018). A better cloud numerical representation is therefore needed to improve climate predictions (e.g., Bodas-Salcedo et al., 2014; Hyder et al., 2018; King et al., 2015).

Fortunately, the 10 year (2013–2022) Polar Prediction Project (PPP, Bromwich et al., 2020) and its intense observational stage, the Year of Polar Prediction (YOPP, 2017–2019), encouraged advanced observational studies that provide more detailed measurements. McFarquhar et al. (2021) describe several field campaigns conducted over the Southern Ocean during 2016–2018. These field campaigns include the Clouds, Aerosols, Precipitation, Radiation, and Atmospheric Composition over the Southern Ocean (CAPRICORN), the Measurements of Aerosols, Radiation, and Clouds over the Southern Ocean (MARCUS), the Macquarie Island Cloud and Radiation Experiment (MICRE), and Southern Ocean Clouds, Radiation, Aerosol Transport Experimental Study (SOCRATES). Our particular interest is in the coastal regions of Antarctica where the U.S. Department of Energy supported a 2015–2017 study of the clouds, radiation, aerosols, and surface energy balance known as the Atmospheric Radiation Experiment (ARM) West Antarctic Radiation Experiment (AWARE, Lubin et al., 2020). Here, we use the advanced observations taken at McMurdo, Antarctica (77°50′47″S and 166°40′06″E) to evaluate simulations with the polar optimized version of the Weather Research and Forecasting (WRF, Skamarock et al., 2008) known as Polar WRF (e.g., Bromwich et al., 2009).

As discussed in Hines et al. (2019), the Antarctic Mesoscale Prediction System (AMPS, Powers et al., 2012) supports scientific field programs over the continent. The AMPS numerical weather prediction forecasts based on the Polar WRF model enable travel to remote sites. Accurate cloud forecasts are important as unpredicted fog and low ceilings can contribute to costly flight mission failures (e.g., Wille et al., 2017). In particular, Pon (2015) showed that the AMPS cloud fraction product needs improvement. Jordan Powers (personal communication, 2021) detailed plans for upgrades to the AMPS cloud forecasts and cloud products that are enabled with improved computing ability from scheduled hardware updates. The authors are collaborating with the AMPS upgrades, and the current Polar WRF work is contributing to these efforts.

The poorly understood contribution, at least until very recently, that aerosols have on the observed behavior of high southern latitude clouds has been a glaring weakness in our ability to well understand and accurately model these clouds (Liu et al., 2018; McFarquhar et al., 2021). The seasonal cycle of aerosols is different in the Antarctic region than over the Arctic, as the winter Arctic haze does not have an analog in the Southern Hemisphere, and Antarctic nuclei number concentrations are an order of magnitude larger during summer than winter (Lachlan-Cope et al., 2020; Liu et al., 2018). An adequate amount of cloud condensation nuclei (CCN) appears to be present to produce common liquid cloud droplet concentrations of 100 cm^{-3} or greater (e.g., Liu et al., 2018). The persistence of the supercooled liquid at McMurdo as observed by Silber et al. (2018) is intriguing. While there has been recent interest in ice particle multiplication in polar clouds and how this might impact amounts of cloud liquid and cloud ice, the best known ice particle multiplication method, the Hallett-Mossop process (HM) is most active for the temperature range −3 to −8°C (Field et al., 2017). Thus, HM might impact relatively warm supercooled clouds. More recently, several studies have considered other processes of secondary ice production (e.g., Fu et al., 2019; Sotiropoulou et al., 2020). Sotiropoulou et al. (2021) suggested another ice multiplication mechanism, breakup from collisions of ice particles, could be active for Antarctic clouds, with peak activity near −15°C. Silber et al. (2018), however, found liquid clouds present at temperature near −30°C during 11 of the 12 months studied. Thus, ice multiplication is not a likely mechanism at these temperatures. Mixed-phase clouds, however, are often unstable due to the lower saturation vapor pressure for ice than for liquid (e.g., Vergara-Temprado et al., 2018). If ice freezing nuclei (INP) are present, glaciation can lead to the decay of the liquid water phase. New observations from CAPRICORN, however, provide an explanation for the persistence of supercooled liquid. INP concentrations were found to be quite low over extensive regions of the Southern Ocean (McCluskey et al., 2018; McFarquhar et al., 2021; Vergara-Temprado et al., 2018). Specifically, McCluskey et al. (2018) found INP concentrations several orders of magnitude lower than earlier values from Bigg (1973). The new findings

seem to correspond with observations to the south over Antarctica that suggested INP concentrations are often sparse (e.g., Grosvenor et al., 2012; Hogan, 1986; O'Shea et al., 2017; Silber et al., 2021). The smaller INP concentrations should slow heterogeneous nucleation of liquid particles and could allow liquid clouds to persist longer. Moreover, Grosvenor et al. (2012) found that mesoscale simulations with several widely used INP parameterizations poorly represented the observed relationship between ice particle concentration and temperature over Antarctica.

Good agreement between observations and model output was recently achieved by Vignon et al. (2021) in regional model simulations with WRF for the Southern Ocean. They adjusted the Morrison microphysics scheme (Morrison et al., 2005) for reduced heterogeneous nucleation consistent with the INP observations of McCluskey et al. (2018) and produced realistic cloud water amounts, while simulations with the unmodified parameterization show a deficit of cloud water. They also examined the impact of vertical resolution and static stability formulation on the supercooled clouds, but found the microphysics parameterization was the primary influence. We apply similar microphysics to a colder domain near the Antarctic coast. Model results are compared to the observations from AWARE described in more detail in Section 2. Section 3 outlines the Polar WRF simulations. Results are discussed in Section 4, and Summary and conclusions are given in Section 5.

2. AWARE Observations

The primary AWARE site was located at McMurdo Station at the southern tip of Antarctica's Ross Island (Figure 1 and Figure S1 in Supporting Information S1) where observations took place between November 2015 and January 2017. The observational data sets from AWARE come from lidars, radars, spectral and broadband radiometers, and remote sensing measurements of Antarctic clouds, combined with aerosol chemical and microphysical sampling equipment, as well as rawinsondes (Lubin et al., 2020). AWARE serves the need for observations that can enable improved numerical simulations, both regional and global, through better representation of Antarctic clouds over a full annual cycle (e.g., Hines et al., 2019).

To produce vertical profiles and time series of cloud properties a cloud mask (derived from detected hydrometeor-bearing air-volumes) determines cloud and liquid occurrence fractions at McMurdo (Silber et al., 2018). We use Ka-band ARM zenith radar (KAZR) and High-Spectral Resolution Lidar (HSRL; Eloranta, 2005) from McMurdo to obtain these fractions. The data were processed as described in Silber et al. (2018). Cloud occurrence is determined on an hourly basis to match the frequency of model output. An hour is attributed as cloudy if the fraction of cloud detections by the beam exceeds 25%. The hour is otherwise "clear." Furthermore, when the detected liquid occurrence fraction exceeds 25% liquid clouds are taken as occurring, with only ice clouds otherwise. Silber et al. (2018) suggest this method may result in an overestimation of up to 3.5% in cloud occurrence fractions on a seasonal basis. The liquid water path is retrieved using microwave radiometer measurements and combined with G-Band Vapor Radiometer Profiler during the November case. The combined product has an uncertainty of 10 g m^{-2}, with the uncertainty otherwise being 25 g m^{-2}. Ice water content is obtained from 35 GHz radar observations following Hogan et al. (2006) and are listed as missing when the cloud fraction is less than 25%. The uncertainty of ice measurements was estimated at 70% by Shupe et al. (2001). We note that the HSRL pulse can occasionally be completely attenuated by optically thick cloud layers (optical thickness greater than 3–5) that can occur synoptically at McMurdo. Furthermore, net longwave and shortwave radiation at the surface radiation are calculated from upwelling and downwelling radiation measurements acquired by the ground radiation radiometers and the sky radiation radiometers. The uncertainty of the observed longwave and shortwave radiation is typically 15 and 4 W m^{-2}, respectively.

3. Polar WRF

WRF has been run in the Antarctic region for several climate and synoptic applications (e.g., Bozkurt et al., 2020, 2021; Bromwich et al., 2013; Deb et al., 2018; Powers et al., 2012). The advanced microphysics capabilities of WRF make it suitable for detailed cloud simulations (e.g., Grosvenor et al., 2012; Hines et al., 2019; Listowski & Lachlan-Cope, 2017; Listowski et al., 2019; Vignon et al., 2021). Polar optimizations are added in Polar WRF (http://www.polarmet.osu.edu/PWRF) to improve the performance for Arctic and Antarctic simulations. Primary Polar WRF modifications adjust the Noah LSM (Barlage et al., 2010) to improve representation of heat transfer through snow and ice (Hines & Bromwich, 2008; Hines et al., 2015). Furthermore, fractional sea

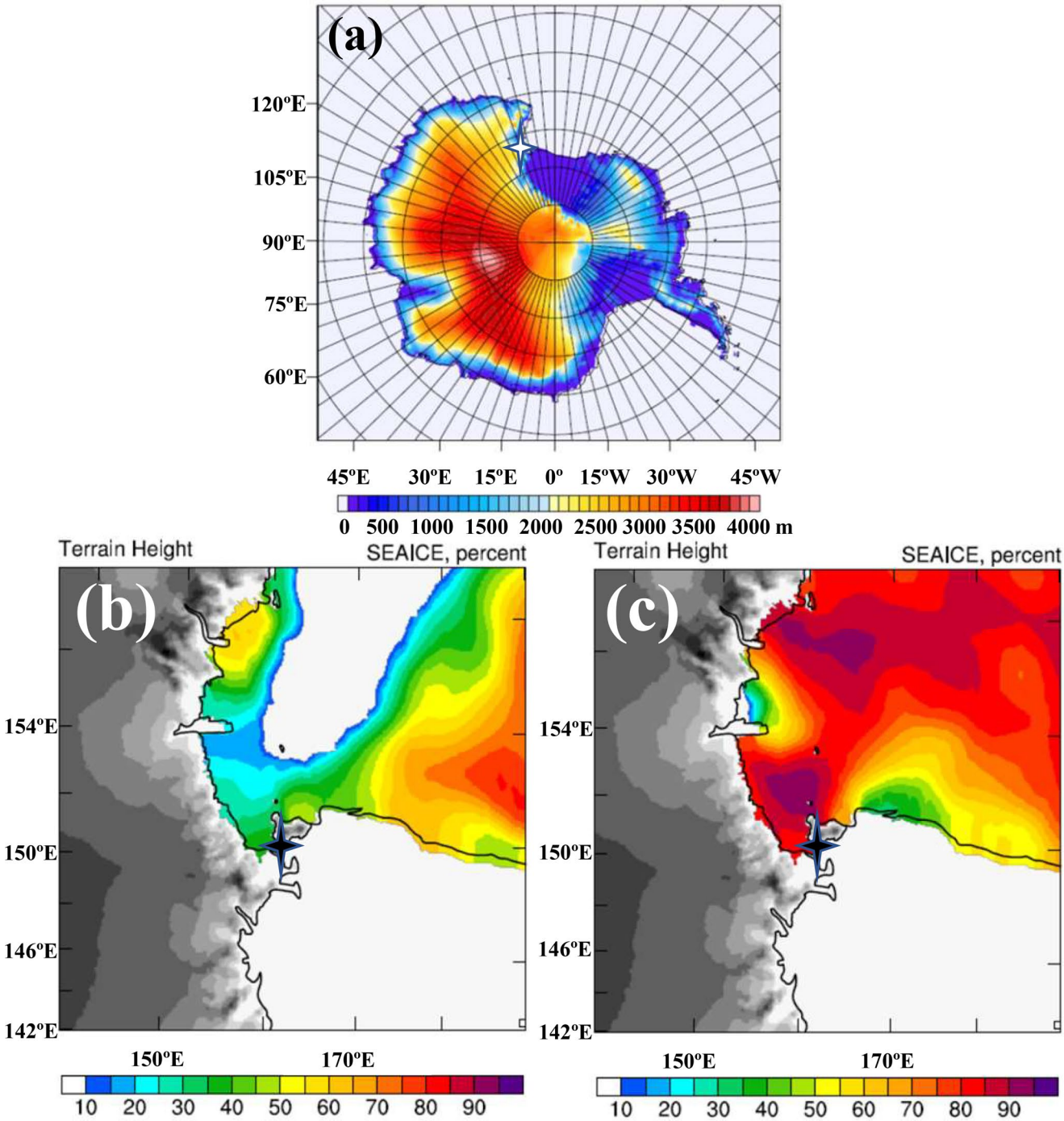

Figure 1. Polar WRF grid for the two-domain Antarctic simulations including (a) the 10-km resolution grid and (b) the 2-km resolution grid with sea ice concentration for 00:00 UTC 10 March 2016 and (c) 00:00 UTC 12 November 2016. Topography (m) is shown by a color scale in (a) and a gray scale in (b and c). Sea ice concentration is shown by a color scale in (b and c). McMurdo is shown by a star.

ice was included by Bromwich et al. (2009), followed by addition of specified variable sea ice thickness, snow depth on sea ice, and sea ice albedo. These updated options were included by the Polar Meteorology Group at Ohio State University's Byrd Polar and Climate Research Center and were ultimately included in the standard release of WRF (https://www.mmm.ucar.edu/weather-research-and-forecasting-model) by collaboration with the Mesoscale and Microscale Meteorology Division at NCAR (Hines et al., 2015) This collaboration is continuing.

For the physical parameterizations, we use past experience with Polar WRF simulations, including those for the Arctic System Reanalysis (Bromwich et al., 2018) and the West Antarctic Ice Sheet (e.g., Hines et al., 2019). We select the Mellor-Yamada-Nakanishi-Niino (MYNN, Nakanishi & Niino, 2006) level-2.5 scheme for the atmospheric boundary layer and surface layer. We use Rapid Radiative Transfer Model for general circulation models (Clough et al., 2005) for longwave and shortwave radiation. Cloud liquid, cloud ice, and snow impact the radiation fluxes, but rain water is not used to calculate radiation. Version 4.1.1 of WRF is used within the Polar WRF simulations.

3.1. Vertical Discretization and Horizontal Gridding

For the model gridding we use 60 vertical levels with the lowest level near 16 m above ground level (AGL) and 12 layers in the lowest 1,000 m AGL. The model top is at 10 hPa. For the horizonal gridding, McMurdo is in complex terrain on Ross Island and mesoscale features are difficult to represent in a modeling study (Figure S1 in Supporting Information S1). Steinhoff et al. (2008) showed that flow in the vicinity of Ross Island is strongly influenced by topographic features on the island, the Transantarctic Mountains to the west and the topography of Ross Ice Shelf region to the south. They also found the Antarctic Mesoscale Prediction System (AMPS) 3.3-km grid provided a credible forecast for most of the Ross Island area.

We use a two-grid representation as shown in Figure 1 and Figure S2 in Supporting Information S1. The outer grid is the same polar stereographic grid used by Hines et al. (2019) with 10 km grid spacing. That grid is 661 points by 641 points and matches a previous AMPS grid. The inner grid has 2 km resolution. We considered using a third interior grid with 400 m resolution to capture the fine details of the Ross Island terrain. However, given the high computational cost of such high-resolution simulations we had selected a different method to capture the circulation near McMurdo.

First, to limit model drift and represent the broader synoptic circulation, grid nudging is added in Polar WRF simulations above model level 32 (above 8,000 m AGL). European Center for Medium-Range Weather Forecasts (ECMWF) fifth-generation reanalysis (ERA5, Hersbach et al., 2020) is used for initial conditions and grid nudging. ERA5 compares favorably to other reanalyses over Antarctica (e.g., Tetzner et al., 2019) and has smaller moisture biases than AMPS (Silber, Verlinde, Wang, et al., 2019). Weak grid nudging is applied for horizontal velocity, temperature, and geopotential with a nudging coefficient of 10^{-4} s^{-1}.

Second, to better represent the flow in the vicinity of McMurdo we use observation nudging to temperature, humidity, and horizontal velocity from twice daily McMurdo rawinsondes and nearby Automatic Weather Station (AWS) observations. Observations every 3 hr from nearby stations of the Antarctic AWS Program (Lazzara et al., 2012) are selected to provide near-surface constraints. Testing indicates that both the soundings and the surface observations impact the simulations. Testing also indicates that the simulation influence by data assimilation still allows the cloud microphysics scheme to maintain its primary influence on simulated cloud statistics. Table S1 in Supporting Information S1 shows the AWS sites used for the data assimilation. The near-surface observations from these AWS are surface pressure, temperature, wind speed, and wind direction. The rawinsonde data are available from the ARM AWARE database for twice daily observations taken slightly after 10:00 and 22:00 UTC. The nudging uses WRF's three-dimensional data assimilation capabilities (Bromwich et al., 2018). Nudging coefficients for geopotential, temperature, wind speed and direction, and specific humidity are set at 6×10^{-4} s^{-1}. Observation nudging is applied on both grids, except for wind that is only nudged on the coarse domain grid to allow the nested grid wind field to respond to the topography. The impact of observation nudging is discussed in Section 4.1.

3.2. Microphysics and the Representation of Clouds

An earlier version of Polar WRF (version 3.5.1) was tested by Deb et al. (2016) over West Antarctica. They found that comparisons of simulated fields to near-surface observations showed that pressure is simulated with high skill, and wind speed is generally well-represented. Weaknesses were found, however, in the diurnal cycle of temperature, especially a cold summertime minimum temperature bias. This was attributed to a negative bias in downwelling longwave radiation, consistent with clouds over Antarctica being poorly represented by models (e.g., Bromwich et al., 2013; Hines et al., 2019; Listowski & Lachlan-Cope, 2017).

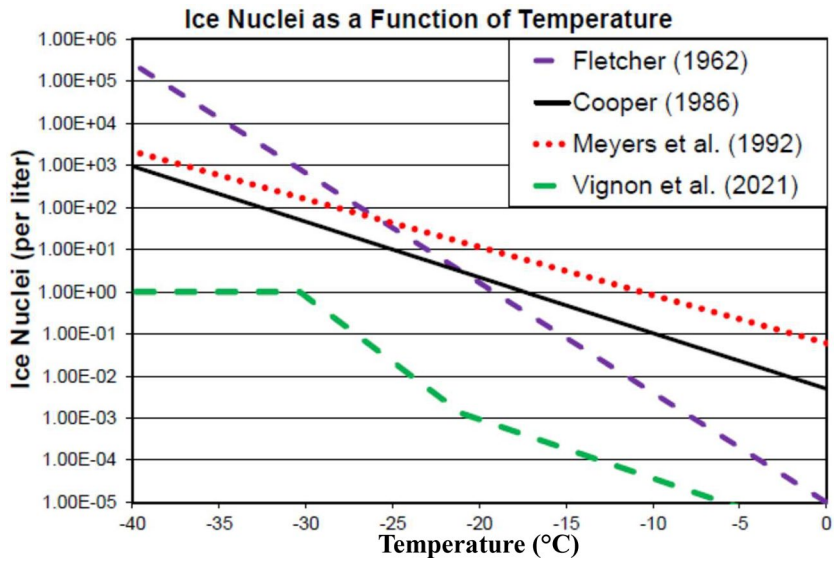

Figure 2. Ice nucleating particle concentration as a function of temperature for several common formulas and the Vignon et al. (2021) Southern Ocean formula.

Accordingly, our focus in this paper is on cloud structure at coastal Antarctica. When we model clouds, low-level clouds frequently have smaller length scales than the model grid spacing (e.g., Jousse et al., 2016). Therefore, we must parameterize clouds. Past studies show more advanced microphysics schemes produce more realistic cloud water over Antarctica (e.g., Hines et al., 2019; Listowski & Lachlan-Cope, 2017). Therefore, the two-moment Morrison-Milbrandt P3 scheme (Morrison & Milbrandt, 2015) is used as it produced more liquid water for simulations of summer clouds over West Antarctica than other schemes, although less than observed cloud water amounts (Hines et al., 2019). The scheme predicts two-moments (number concentration and condensate mixing ratio) for ice condensate and thus provides a more robust treatment of particle size distributions that are important for microphysical process rates and cloud/precipitation evolution. We use the version of P3 with one ice category. The P3 scheme avoids the arbitrary categorization of frozen hydrometeors into cloud and precipitation, and thus allows for a continuum of particle properties. Ice variables include total mass, number concentration, rime mass, and rime volume, allowing for four degrees of freedom. Liquid hydrometeors use a standard approach with cloud and rain categories. The standard setting for the liquid droplet number, 200 cm^{-3}, is used for the simulations discussed in Section 4. This setting is reasonable given observed CCN concentrations during AWARE (Lubin et al., 2020). The impact of the setting is discussed in the supplement (see Figure S6 in Supporting Information S1). A smaller liquid droplet number did not consistently increase or decrease the liquid water path, and the impact on the simulations was minor.

Two applications of the ice physics within the P3 scheme are used here. The standard settings allow cloud water and rain to freeze and form cloud ice by several processes. At temperatures below −40°C, the homogeneous freezing of droplets occurs without the necessity of INP. For temperature below −4°C immersion freezing of both cloud liquid and rain occurs according to the formulation of Bigg (1953). In the Morrison microphysics scheme, the INP concentrations were specified by the Meyers et al. (1992) curve, but for P3 the INP concentrations are not explicitly specified in the formulation. The rate of freezing, however, is enhanced at lower temperatures, consistent with large activable INP concentrations. Contact freezing is included in the earlier Morrison et al. (2005) scheme that is a WRF option, but contact freezing is not included in P3. Freezing nucleation occurs for temperature less than −15°C when ice supersaturation exceeds 5%. Ice formation could be reduced by increasing the supersaturation threshold, and supersaturation is more likely to occur in pristine environments. A more physical approach, however, to setting the freezing nucleation is based upon INP concentration. The standard model setting is based on the INP formulation of Cooper (1986) that greatly increases the activable INP concentration as temperature decreases (Figure 2).

Table 1
List of Polar WRF Simulations for 2016

Run name	Time period	Microphysics scheme	Data assimilation
ControlM	5–11 March 2016	P3—standard	Yes
ControlN	5–14 November 2016	P3—standard	Yes
No Data Assimilation	5–14 November 2016	P3—standard	No
No IceM	5–11 March 2016	P3—no freezing of cloud water $T > -40$°C	Yes
No IceN	10–12 November 2016	P3—no freezing of cloud water $T > -40$°C	Yes
VignonM	5–11 March 2016	P3—Vignon ice nuclei	Yes
VignonN	10–14 November 2016	P3—Vignon ice nuclei	Yes
FallLiq	5–11 March 2016	P3—Vignon ice nuclei and fall setting for liquid droplet number	Yes
SpringLiq	10–14 November 2016	P3—Vignon ice nuclei and spring setting for liquid droplet number	Yes
FebMar Control	1 February to 31 March 2016	P3—standard	Yes
FebMar Vignon	1 February to 31 March 2016	P3—Vignon ice nuclei	Yes

Vignon et al. (2021) created an alternative formulation of the Morrison microphysics for the Southern Ocean based upon the INP observations of McCluskey et al. (2018). The INP concentration in number per liter, A_i, is given by Vignon et al. with the formulation,

$$\log_{10}\left(A_i\right) = 0 \quad \text{for } T \le T_1 \tag{1}$$

$$\log_{10}\left(A_i\right) = -0.31\left(T - T_o\right) - 2.88 \quad \text{for } T > T_1 \text{ and } T \le T_o \tag{2}$$

$$\log_{10}\left(A_i\right) = -0.14\left(T - T_o\right) - 2.88 \quad \text{for } T > T_o \tag{3}$$

where T is temperature, T_1 is −30.35°C, and T_o is −21.06°C. The resulting INP concentration is shown in Figure 2. At realistic cloud temperatures, the INP can be three orders of magnitude less than commonly used values from Fletcher (1962), Cooper (1986), and Meyers et al. (1992).

The revised microphysics can be implemented into either the Morrison or the P3 schemes. Immersion freezing is still allowed for rain particles, which tend to be larger, but is not allowed for cloud water particles, which are typically more numerous in simulations with the Morrison and P3 schemes (Hines et al., 2019). Vignon et al. (2021) removed contact freezing from the revised Morrison scheme. For freezing nucleation, the rate of production of cloud ice particles due to freezing is given as the following,

$$\frac{DN_i}{Dt} = \left(A_i - N_i\right)\frac{1}{\Delta t} \tag{4}$$

where N_i is the number concentration of cloud ice, t is time, Δt is the time step, and the rate of change due to freezing is not allowed to be negative. The small values of A_i in the revised parameterization slow the production of ice particles and allow liquid to persist longer. While Vignon et al. (2021) installed these changes in the Morrison microphysics, we adapted the changes to the P3 scheme for some of our simulations (Table 1), which include very cold supercooled clouds.

3.3. Cases

We select two supercooled case study periods (5–11 March 2016 and 5–14 November 2016) when atmospheric observations indicated the presence of liquid hydrometeors at air temperatures near −30°C at McMurdo. These cases are challenging to simulate, since models typically remove any liquid by glaciation at this temperature. We benefit from Silber et al. (2018) and Silber, Verlinde, Cadeddu, et al. (2019) who produced cloud and radiation data sets for McMurdo during 2016.

For the model output, we select the nearest land grid point adjacent to McMurdo for comparison to the AWARE observations. We run 36-hr segments starting at 00:00 UTC each day, then patch together hours 12–35 to obtain hourly results. This allows adequate spin-up time of the boundary layer and hydrology and reduces the gradual model drift (e.g., Hines et al., 2019).

To detail the synoptic conditions near McMurdo during the case studies, we select fields from the AMPS archive (http://polarmet.osu.edu/AMPS/ or https://www2.mmm.ucar.edu/rt/amps/information/amps). Figure S3 in Supporting Information S1 shows 6-hr forecasts of near-surface fields from AMPS grid 3 with 3.3 km grid spacing, which has a somewhat larger domain than our inner grid with 2-km resolution (Figure S2 in Supporting Information S1).

Simulated near-surface atmospheric fields during these time periods for AMPS grid 3 are impacted by the robust local topography on Ross Island and the Ross Ice Shelf airstream (e.g., Seefeldt & Cassano, 2012). The near-surface temperatures during March over the Ross Ice Shelf are below −20°C, with warmer air over the Ross Sea to the north. In addition to the near-surface fields shown in Figure S3 of Supporting Information S1, the middle-tropospheric fields at 500 hPa are shown in Figure S4 of Supporting Information S1. At 500 hPa, there is a low near McMurdo at 06:00 UTC on 11 March (Figure S4b in Supporting Information S1). For the November case, there is a trough with cyclonic (clockwise) turning in the region at 06:00 UTC on 9 November that widens into a broader cyclonic feature on 06:00 UTC 12 November (Figures S4c and S4d in Supporting Information S1). Therefore, the synoptic and mesoscale features may be favorable for cloud formation near Ross Island during the March and November study periods. The 500 hPa temperature field in Figure S4 of Supporting Information S1 is not well-aligned with the 500 hPa contours, thus thermal advection is occurring. Accordingly, the synoptic and mesoscale structures are evolving during March and November cases, rather than a stable and slowly evolving equivalent barotropic structure. The cold temperatures displayed in Figures S3 and S4 of Supporting Information S1 are associated with small water vapor and hydrometeor contents (e.g., Miao et al., 2001).

As the supercooled cases in March and November 2016 provide limited examples of the synoptic conditions observed at McMurdo, we also conduct 36-hr simulation segments initialized every day at 00:00 UTC for 1 February 2016 to 30 March 2016 (Table 1). Extensive cloud liquid and cloud ice was observed during this 2 month period. Hours 12–35 (and 12:00 UTC on 31 March) of the segments were combined. This provides a statistical database over multiple synoptic events, not just the cold supercooled cases.

4. Results

4.1. Impact of Data Assimilation on Model Results

We investigated the impact of the assimilation of the rawinsondes and the AWS observations with a study of the November case. Our ultimate goal is not an independent evaluation of the model meteorological fields in comparison to observations, but to represent the conditions under which clouds develop along coastal Antarctica. A simulation with data assimilation to both the McMurdo rawinsondes and nearby AWS observations is compared to a simulation with no data assimilation. Figure 3 shows vertical profiles of the data assimilation and no data assimilation simulations for a selected time, 10:00 UTC 13 November 2016. Rawinsonde profiles from 10:17 UTC are used to compare with the model results. For temperature and dew point temperature, the data assimilation run values are much closer to the observed values (the solid curves), while the simulation without data assimilation (red curves) shows much larger errors (Figure 3a). In particular, the simulation without data assimilation is much dryer, so the dew point temperature is several degrees lower than that observed. The dryness is also seen in the specific humidity profile (Figure 3c). The dryness of the atmosphere without mesoscale data assimilation may result from a general dryness of the atmosphere in Antarctic latitudes for ERA5, which is used for the initial conditions (Silber, Verlinde, Wang, et al., 2019). The data assimilation is not effective in correcting errors in the wind speed and wind direction profiles (Figure 3b). A better resolution of the terrain features near McMurdo could improve the wind simulation there.

Time series for the November case also demonstrate the impact of the data assimilation (Figure 4). The precipitable water vapor, PWV, can be determined from the column water vapor,

$$\mathrm{PWV} = \int_0^\infty \rho\, q\, dz \tag{5}$$

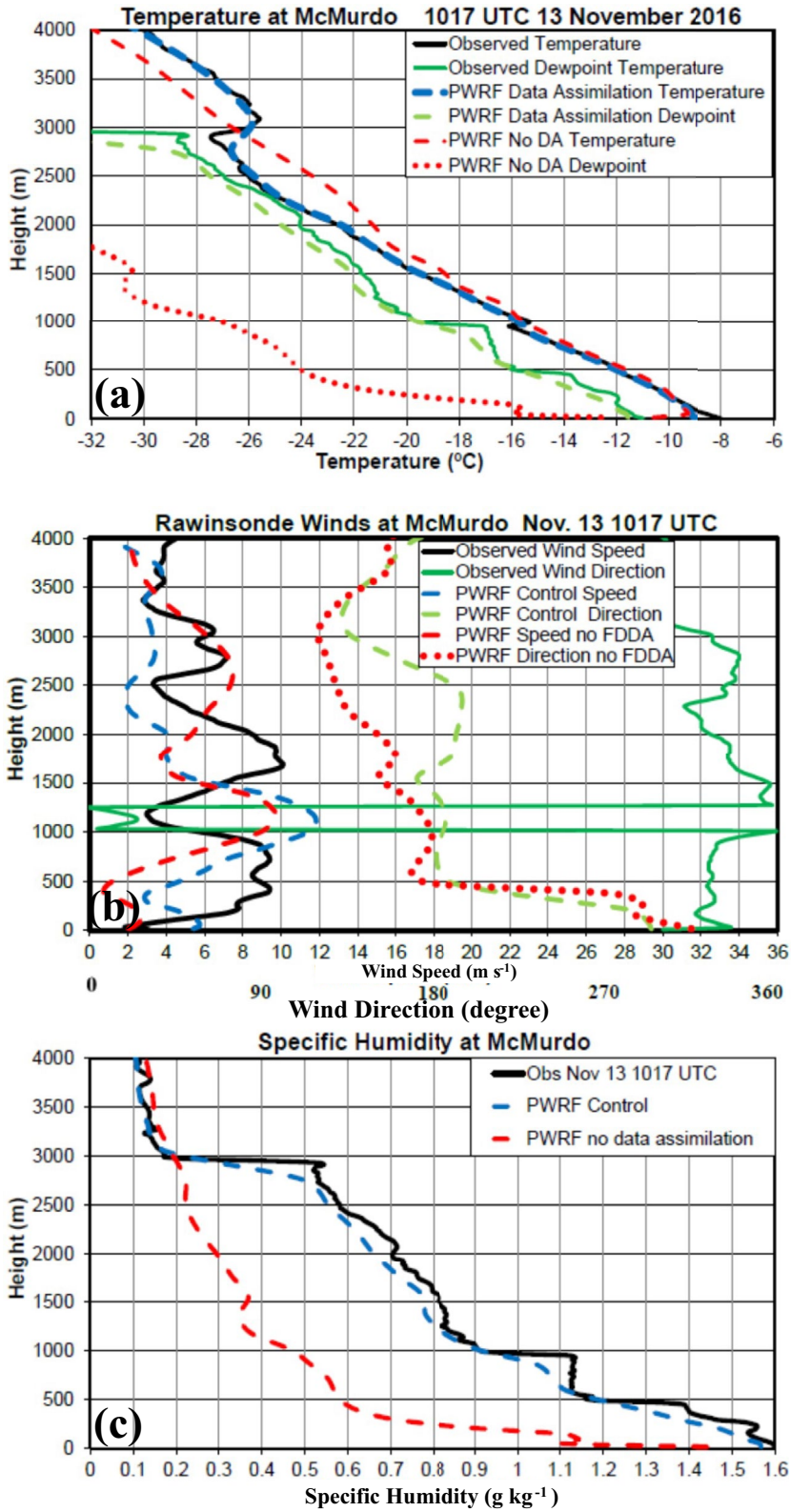

Figure 3. Vertical profiles of observed fields, the Polar WRF simulation with data assimilation (Control) and the No Data Assimilation Polar WRF simulation at 10:17 UTC 13 November 2016 for (a) temperature (°C) and dew point temperature (°C), (b) wind speed (m s^{-1}) and wind direction (degrees), and (c) specific humidity (g kg^{-1}). Wind direction cycles between 0 and 360°.

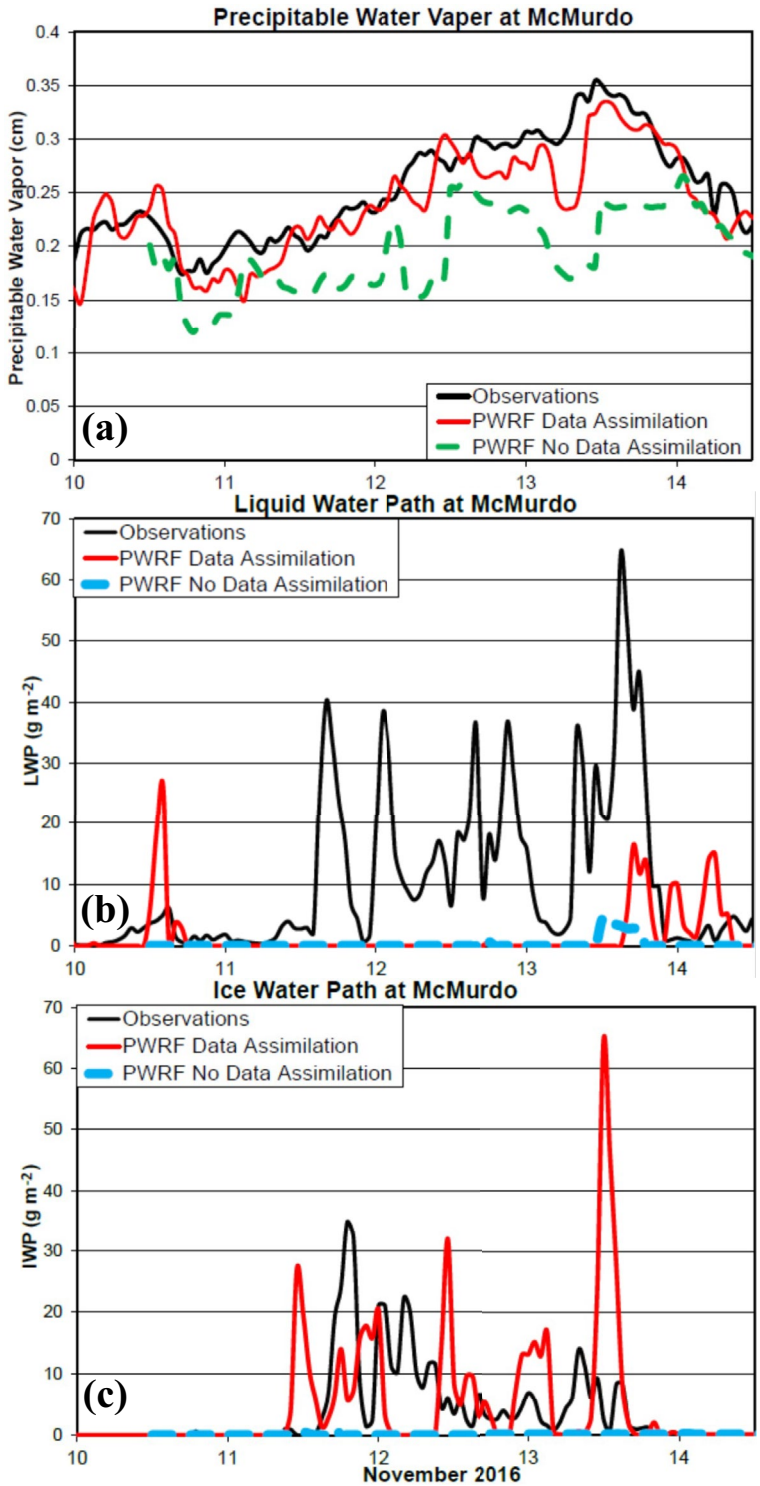

Figure 4. Time series of (a) precipitable water vapor (cm), (b) liquid water path (g m^{-2}), and (c) ice water path (g m^{-2}) for 00:00 UTC 10 November 2016 to 12:00 UTC 14 November 2016 for observations (solid black curve), the data assimilations simulation (red curve) and the No Data Assimilation simulation (dashed blue curve).

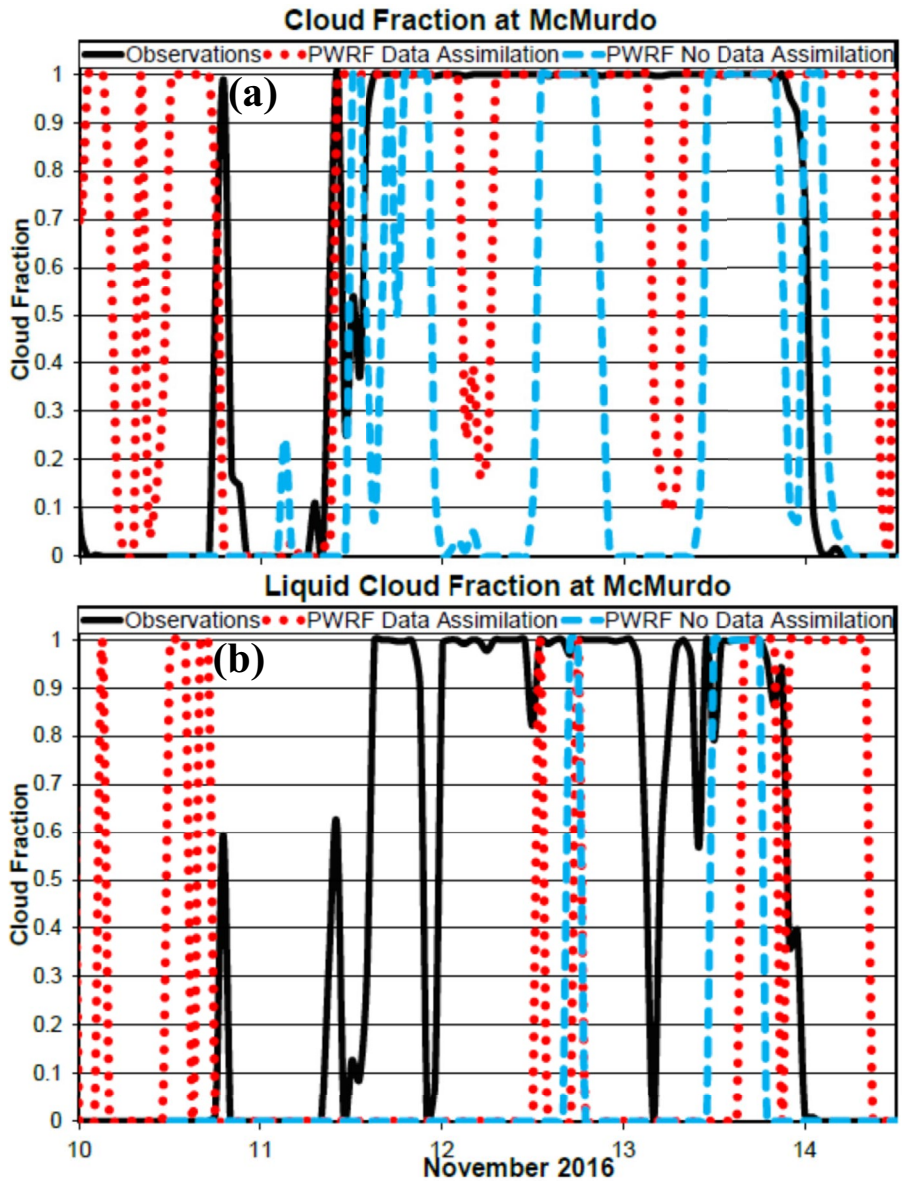

Figure 5. Time series of (a) total cloud fraction and (b) liquid cloud fraction for 00:00 UTC 10 November to 12:00 UTC 14 November 2016 for observations (solid black curve), the Data Assimilation simulation (dashed red curve) and the No Data Assimilation simulation (dashed blue curve).

where ρ is the air density, q is specific humidity, and z is height. The PWV is considerably less in the simulation without data assimilation (Figure 4a). The average observed value during 00:00 UTC 11 November to 00:00 UTC 14 November 2016 is 0.27 cm. It is slightly less in the simulation with data assimilation, 0.25 cm, and considerably less, 0.20 cm, for No Data Assimilation. Thus, Data Assimilation has less water vapor than the observations, but more than No Data Assimilation. Over the same time period used for the precipitable water vapor averages, the liquid water path averages are 15.1 g m^{-2} for the observations, 1.0 g m^{-2} for Data Assimilation, and just 0.4 g m^{-2} for the driest simulation. These average simulated values vary within the uncertainty for observed liquid water path. Data Assimilation produces more ice water path than the observations, but No Data Assimilation produces almost no ice water path (Figure 4c).

We use the observations of total cloud fraction and liquid cloud fraction according to the Silber et al. (2018) detection algorithm for comparison with the simulations (Figure 5). Observed clouds are present over the great majority of the hours during 00:00 UTC 11 November to 00:00 UTC 14 November 2016 (Figure 5a). Average

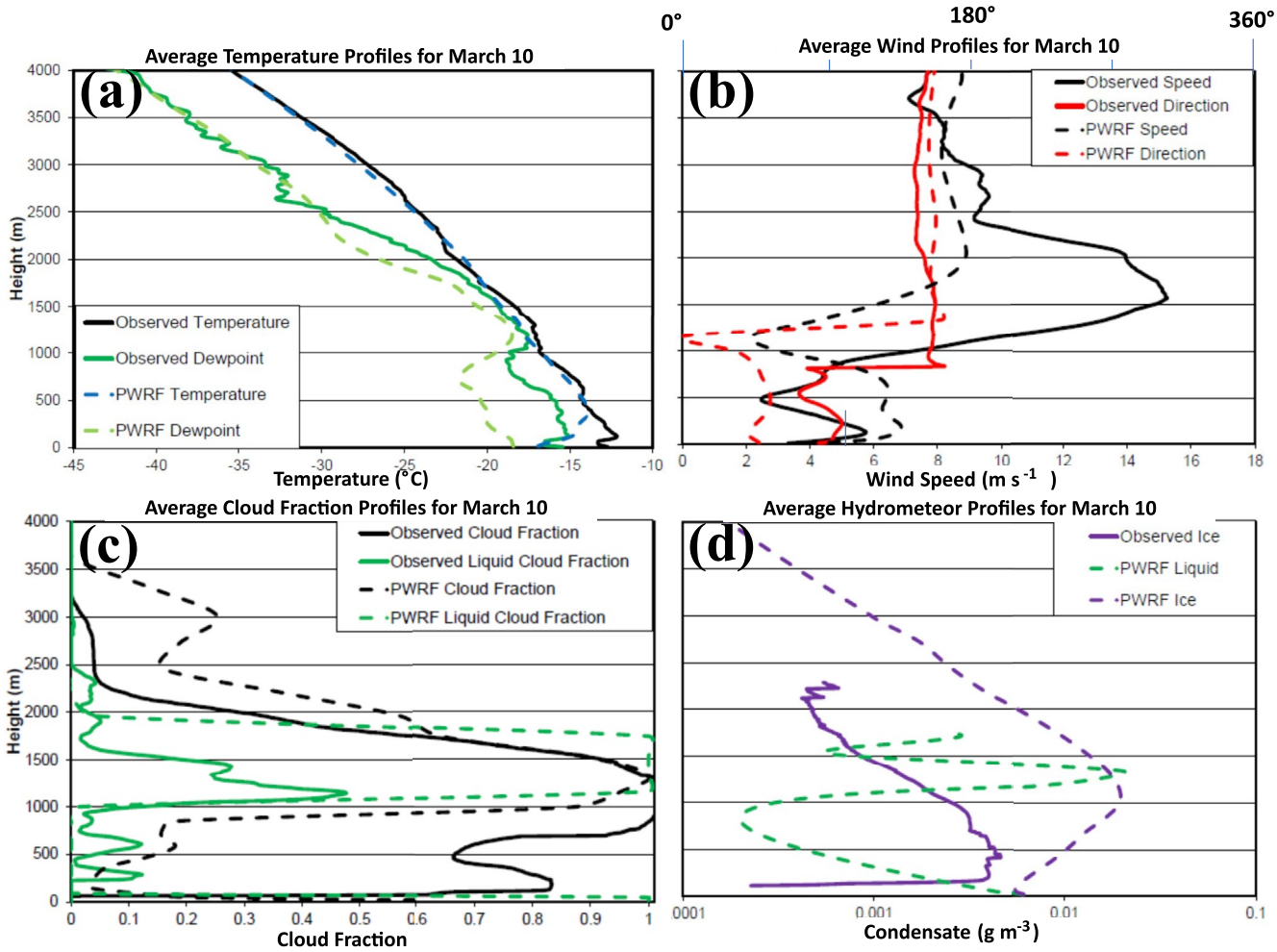

Figure 6. Vertical profiles of observed and simulated fields averaged over 10 March 2016 for (a) temperature (°C) and dew point temperature, (°C) (b) wind speed (m s^{-1}) and wind direction (degrees), (c) cloud fraction and liquid cloud fraction, and (d) liquid water content and ice water content (g m^{-3}).

observed cloud fraction is 84.1% during this time. Average liquid cloud fraction was 71.1%. For the simulations, WRF uses a threshold of 10^{-6} kg per kg of air for the hydrometeor mixing ratio to identify clouds at a point in space and time. The liquid cloud fraction is relatively insensitive to the specification of the threshold, but because ice clouds are often diffuse many ice clouds have a hydrometeor mixing ratio less than 10^{-5}. We set the cloud fraction at zero for hydrometeor mixing ratio less than the threshold. Thus defined, the average simulated cloud fraction for Data Assimilation was 77.8% and 40.5% for No Data Assimilation. Thus, the assimilation increases the total cloud fraction to near the observed value. Modeled liquid cloud fractions, however, average less than 0.15 and are much less than the observed value. The results shown in Figures 3–5 demonstrate that it is critical to have data assimilation to increase the water vapor in our simulations to represent the Antarctic clouds. Mesoscale data assimilation may be an essential tool for cloud modeling studies in the future. For the remainder of this work we refer to the simulation with data assimilation as the ControlN (Table 1).

4.2. Vertical Profiles

Figure 6 shows the 24-hr averages for 10 March. Temperature, dew point temperature, wind speed, wind direction, total cloud fraction, liquid cloud fraction, and condensed liquid and ice are shown for both observations and the ControlM run. The closeness of the temperature and dew point profiles suggests clouds may occur between 1,000 and 1,800 m AGL (Figure 6a). This corresponds well to the model cloud fraction (Figure 6c), however, the highest average cloud fraction for the observations is located over a slightly lower range between 800 and 1,500 m

AGL. Some cloud liquid is observed between 1,000 and 1,500 m AGL, and this is also seen in the model results (Figure 6c). Fractional liquid cloud is commonly listed for the remote sensing observations organized into hourly averages, but values in-between 0 and 1 are uncommon for the model output. This impacts the liquid profiles in Figure 6c. Notice that the maximum observed liquid cloud fraction, above 1,000 m AGL, is located above the maximum in ice water content just below 500 m (Figure 6d). The maximum simulated liquid water content is also slightly above the maximum simulated ice water content (Figure 6d). The observed wind speed profile is not well-represented by the model (Figure 6b). The wind speed maximum near 1,500 m is only weakly present in the simulation and is located 500 m too high. The wind direction profile is better represented by the model (Figure 6b). The complex terrain near Ross Island could be responsible for the difficulty in representing the wind profile in the lower half of the troposphere.

A comparison of the observed versus modeled ice water content profile indicates that the model is simulating too much ice (Figure 6d). Observed liquid water content profiles are not available. The excess in simulated ice is confirmed when we compare the vertically integrated ice water path between the simulation and the observations. The observed ice water path for 10 March is 3.65 g m^{-2}, but the simulated value is an order of magnitude larger, 27.74 g m^{-2}, outside the retrieval uncertainty range (not shown). Conversely, the observed (supercooled) liquid water path is 69.35 g m^{-2}, while the simulated value is an order of magnitude smaller at 5.68 g m^{-2}.

The 24-hr averages on 13 November are shown in Figure S5 of Supporting Information S1 and are analogous to the March 10 values shown in Figure 6. The temperature and dew point temperature profiles in Figure S5a of Supporting Information S1 suggest clouds are possible below 2,500 m AGL, with a dryer level above that. Figure S5c in Supporting Information S1 shows that the observed cloud fraction actually extend up to 3,000 m, while a layer of simulated cloud has a similar cloud top. The Control simulation simulates some liquid water below 400 m (Figures S5c and S5d in Supporting Information S1) while some liquid fraction is observed below 1,600 m, with a higher layer of observed liquid fraction below 3,000 m. The simulated ice water content is too large above 1,000 m (Figure S5d in Supporting Information S1), consistent with the simulated cloud fraction peaking near 2,200 m, while the observed cloud fraction peaks near 700 m. The observed precipitable water vapor on this day is 0.32 cm, while the simulated amount is 0.29 cm, within 10% of the observed value. The observed liquid water path, 19.81 g m^{-2}, is again an order of magnitude larger than that simulated, 2.61 g m^{-2}. The observed ice water path is 3.91 g m^{-2}, while that simulated is larger at 9.87 g m^{-2}. For both test periods, the model is simulating too much ice and not enough supercooled liquid.

4.3. Sensitivity Simulations With Modified Ice Physics

In previous work, Hines and Bromwich (2017) found that change, consistent with small CCN, to the specified liquid droplet concentrations in the Morrison microphysics improved the simulation of cloud water over the Arctic Ocean by Polar WRF. However, the low-level Arctic clouds during the Arctic Summer Ocean Cloud Study (ASCOS) period considered were relatively warm with typical low cloud temperatures at or slightly below the freezing point. Thus, glaciation was not an efficient process at removing cloud liquid water, and the ice physics was not a controlling factor in the simulation of liquid. For the current case studies, however, supercooled liquid is present at much lower temperatures, and hence ice physics is likely to be a primary factor. As mentioned previously, liquid particles compete unfavorably with any ice particles present over the range of observed temperatures during the March and November cases. We surmise that some factor must be limiting the growth of ice particles, thus allowing the persistence of liquid clouds. Unfortunately, ice physics is still less well understood than liquid-phase physics (e.g., Morrison & Milbrandt, 2015).

We ran two sensitivity tests for each test period and the simulations are listed in Table 1. First, we ran a sensitivity test in which we removed the primary sources of ice nucleation in the P3 scheme, except for homogeneous nucleation at temperature less than −40°C and the immersion freezing of rain drops at temperature below −4°C. The supercooled rain mixing ratio is typically much smaller than supercooled cloud water mixing ratio at temperatures much below freezing in simulations with the P3 scheme (e.g., Hines et al., 2019), so freezing of rain is unlikely to be a major source of ice. These new simulations for March and November are called “No IceM” and “No IceN,” respectively.

The second set of tests is based upon the adapted Vignon et al. (2021) parameterization for P3 as given in Section 3. These March and November simulations are called “VignonM” and “VignonN,” respectively. The time

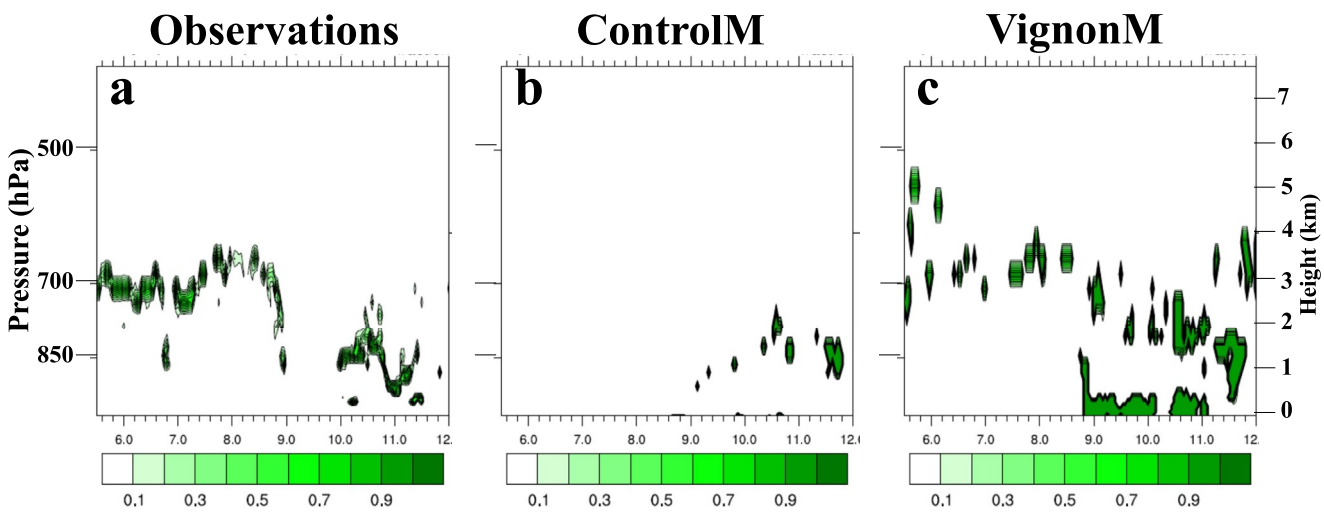

Figure 7. Time evolution of the vertical profiles of liquid cloud fraction for (a) the observations, (b) ControlM, and (c) VignonM. Day of March is the abscissa.

evolution of liquid cloud fraction for VignonM is compared to ControlM and the observations in Figure 7. The figure demonstrates that liquid is typically not observed in deep layers (Figure 7a). Instead, liquid occurs in thin layers near cloud top (e.g., Vignon et al., 2021). The sensitivity test VignonM with Polar WRF is much more successful at capturing cloud water than ControlM (Figures 7b and 7c). The near-surface liquid cloud seen in Figure 7c could be related to the cold bias seen in Figure 6a.

For comparison, the observations provide a time series of vertically integrated fields and vertical profiles of liquid cloud fraction and ice water content. Figure 8 shows vertical profiles of the observed and simulated fields, including the sensitivity tests. The fields are averaged for each of two time periods. Some observed fields were missing during 9 March 2016, so we averaged over 12:00 UTC 5 March to 12:00 UTC 11 March 2016, excluding values from 9 March. The second time period is 12:00 UTC 10 November to 12:00 UTC 14 November 2016.

The maximum value for observed total cloud fraction (not shown) is at 1,250 m AGL for the March period and 1,400 m AGL for the November period. Thus, the elevated observed liquid cloud fraction maxima shown in Figures 8a and 8b are consistent with a liquid cloud layer near the cloud top, in accord with Figure 6 and observations of cloud top liquid layers over the Arctic and Southern Ocean. In contrast, the observed ice water contents vary less below 2,500 m (Figures 8c and 8d).

A double maximum for observed liquid could fraction is seen in Figure 8a at 2,850 and 2,400 m AGL, while the sensitivity tests show a single maximum at roughly similar heights. The observed maximum of about 0.15 near 2,450 m AGL in Figure 8b is well-replicated in the No IceN and VignonN sensitivity tests. In contrast, the ControlM and ControlN poorly represent the liquid cloud fraction. It is clear that the changes to the ice microphysics in the sensitivity tests produce a much improved simulation of the liquid fraction profile. The simulations also produce a near-surface liquid cloud layer that is not apparent in the observations.

For ice water content, ControlM and ControlN produce much larger values than the sensitivity tests (Figures 8c and 8d). The difference can be one order of magnitude or more. The Control values often exceed the observed ice water content, while the sensitivity tests tend to produce less than the observed values. Figure 8 suggests it can be difficult to simulate proper amounts of cloud ice and cloud liquid at the same time, however, the observational uncertainty limits our ability to make firm conclusions. The Vignon simulations appear to best balance simulation of both ice and liquid.

Time series of condensate water contents is shown in Figure 9. None of the simulations well-match the hourly variations of the observations, however, liquid condensate is increased and ice condensate is decreased in the sensitivity simulations. For the March case, we consider hydrometeors for the time period from 12:00 UTC March 8 to 12:00 UTC March 11 when clouds were very frequently observed at McMurdo. The averages for precipitable water vapor in the observations, the ControlM, No IceM, and VignonM during this period are 0.27, 0.30, 0.30, and 0.30 cm, respectively. For the liquid water path, the values are 70.14, 2.59, 86.44, and 61.34 g m^{-2},

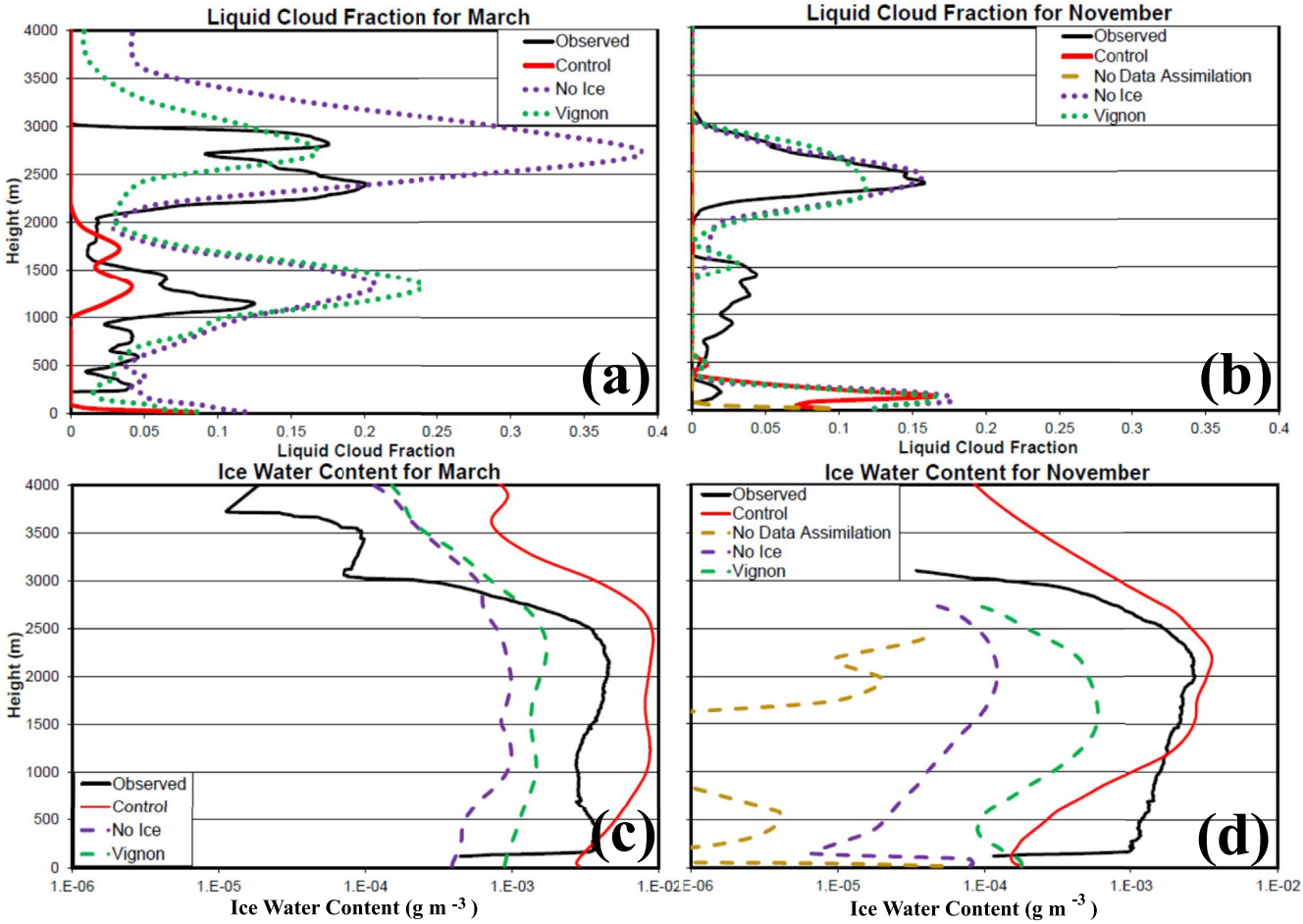

Figure 8. Vertical profiles of observed and simulated fields averaged over 12:00 UTC 5 March to 12:00 UTC 11 March 2016, except 9 March for (a and c) and 12:00 UTC 10 November to 12:00 UTC 14 March 2016 for (b and d). (a and b) Liquid cloud fraction and (c and d) ice water content (g m^{-3}).

respectively. For the ice water path, the values are 22.95, 26.91, 3.41, and 4.30 g m^{-2}, respectively. The sensitivity tests produce realistic amounts of liquid, with VignonM producing slightly less liquid and slightly more ice condensate than No Ice. For the November case we look at averages for 00:00 UTC 11 November to 00:00 UTC 14 November when clouds were extensive. For the observations, the ControlN, No IceN, and VignonN, the precipitable water vapor averages 0.27, 0.25, 0.26, and 0.28 cm, respectively. For liquid water path, the values are 15.08, 1.00, 10.99, and 10.62 g m^{-2}, respectively. For ice water path, the values are 6.67, 7.19, 0.25, and 1.15 g m^{-2}, respectively. The adjustments in our sensitivity tests improve the amounts of liquid simulated, but also result in too little ice. Simulating both the correct amount of supercooled liquid and ice in the clouds remains a challenge.

Figure 10 displays times series of near-surface temperature, wind speed, and direction. The ice physics changes in the sensitivity tests produce more realistic simulations of near-surface temperature, which is often warmer in the tests than in the control simulations (Figures 10a and 10b). During 12:00 UTC 10 November to 12:00 UTC 14 November, average observed near-surface temperature is −8.8°C. Average simulation biases for this time period vary from −3 to −2°C, with the bias having greater magnitude for the controls and reduced magnitude for the sensitivity tests. During 12:00 UTC 5 March to 12:00 UTC 11 March, the average observed temperature is −15.0°C, and the biases are slightly smaller in magnitude than during November. On the other hand, the sensitivity tests do not generally show improvement in the simulation of low-level wind speed and wind direction (Figures 10c–10f). The wind field errors may be because the cloud impacts on the thermodynamic fields are more direct than those on the kinematic fields.

Figure 11 shows time series of downwelling longwave and shortwave radiation at the surface. The changes to the ice physics in the sensitivity tests tend to increase the downwelling longwave radiation and reduce the downwelling

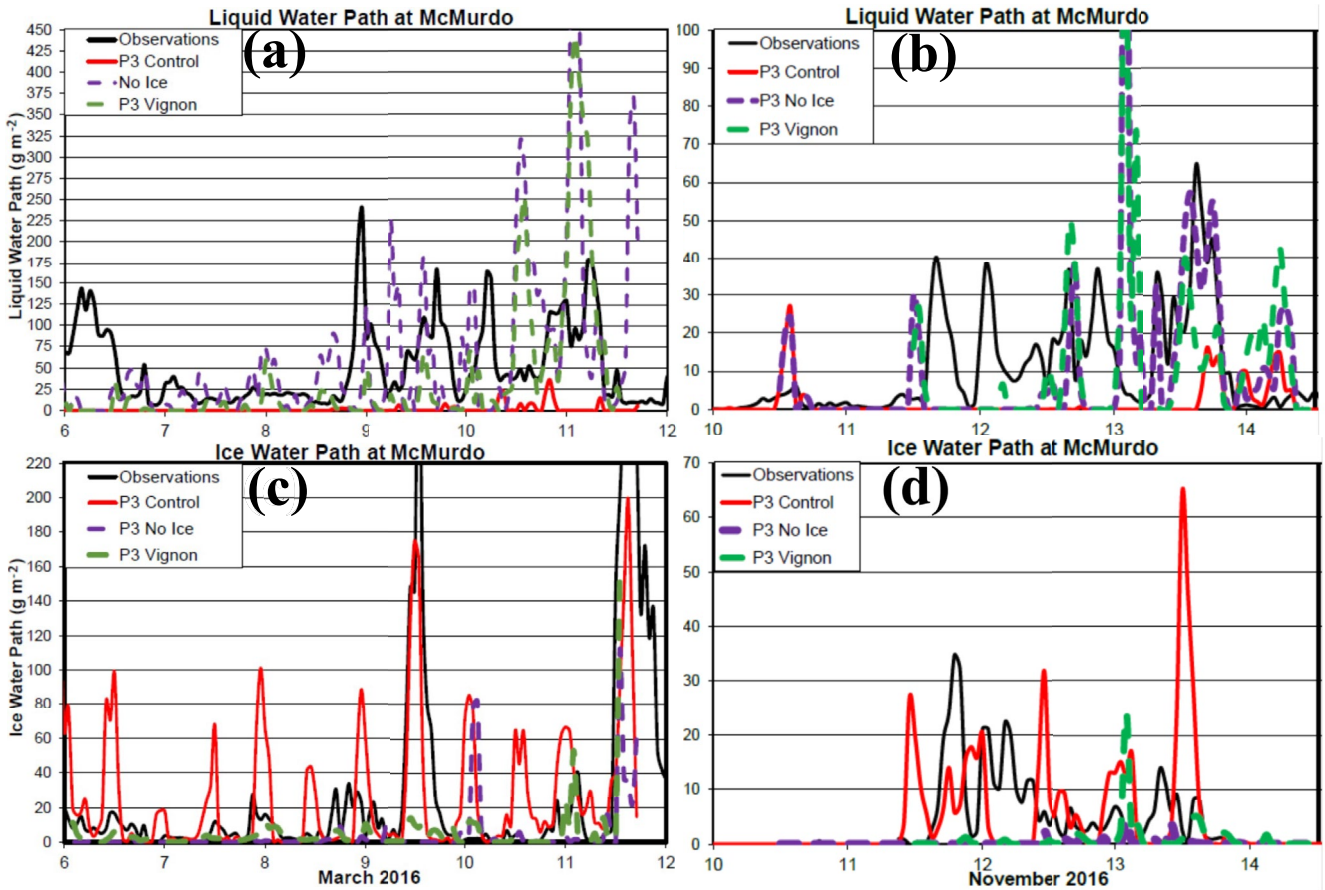

Figure 9. Time series of liquid water path (g m^{-2}) for (a) March 2016, and (b) November 2016, and ice water path (g m^{-2}) for (c) March 2016, and (d) November 2016. Observations are shown by solid black curves, while the Control simulations are shown by the solid red curves. The sensitivity simulations for the No Ice and Vignon sensitivity tests are shown by the dashed purple and green curves, respectively.

shortwave radiation. The change is emphasized for downwelling shortwave on 11 March (Figure 11a). The difficulty in capturing the high-frequency variability of the clouds, however, influences the downwelling longwave seen in Figure 11c. Overall, the ice physics modifications improve the simulations. We calculated biases for 12:00 UTC 5 March to 12:00 UTC 11 March and for 12:00 UTC 10 November to 12:00 UTC 14 November. The shortwave biases were largest for ControlM and ControlN, 43.7 and 35.2 W m^{-2} for the March and November cases, respectively. They were reduced to 17.6 and 3.7 W m^{-2}, respectively for No IceM and No IceN, and 26.9 and 2.3 W m^{-2}, respectively for VignonM and VignonN. The biases of the simulations were sometimes positive and sometimes negative for the downwelling longwave radiation. The longwave biases were always negative for the controls, −18.9 and −7.7 W m^{-2} for the March and November cases, respectively. The smallest magnitude longwave bias for March (−0.5 W m^{-2}) was for VignonM. The smallest bias for November (6.0 W m^{-2}) was for No IceN.

The March and November cases include very cold supercooled liquid cases and show that changes to the microphysics can improve the simulation of liquid for these cases. For a more general evaluation of how microphysics changes impact simulations for McMurdor, Table 2 displays statistics for the February to March simulations. The statistics are calculated for 12:00 UTC 1 February to 12:00 UTC 31 March. The numbers in parenthesis are the uncertainty for the observations and for the simulations shown is the difference corresponding to $t = 2$ for the t-test. Only a control case with standard P3 settings and a Vignon setting case are considered. The Control simulates less liquid cloud fraction and liquid water path than the observations. The change to the Vignon setting increases both liquid fraction and liquid water path. It is possible that secondary ice production not represented in the simulations (see Sotiropoulou et al., 2021) could occasionally increase the ice amounts in the observations, as with the Vingon setting the model simulates slightly less ice than observed over the 2-month period. The cloud

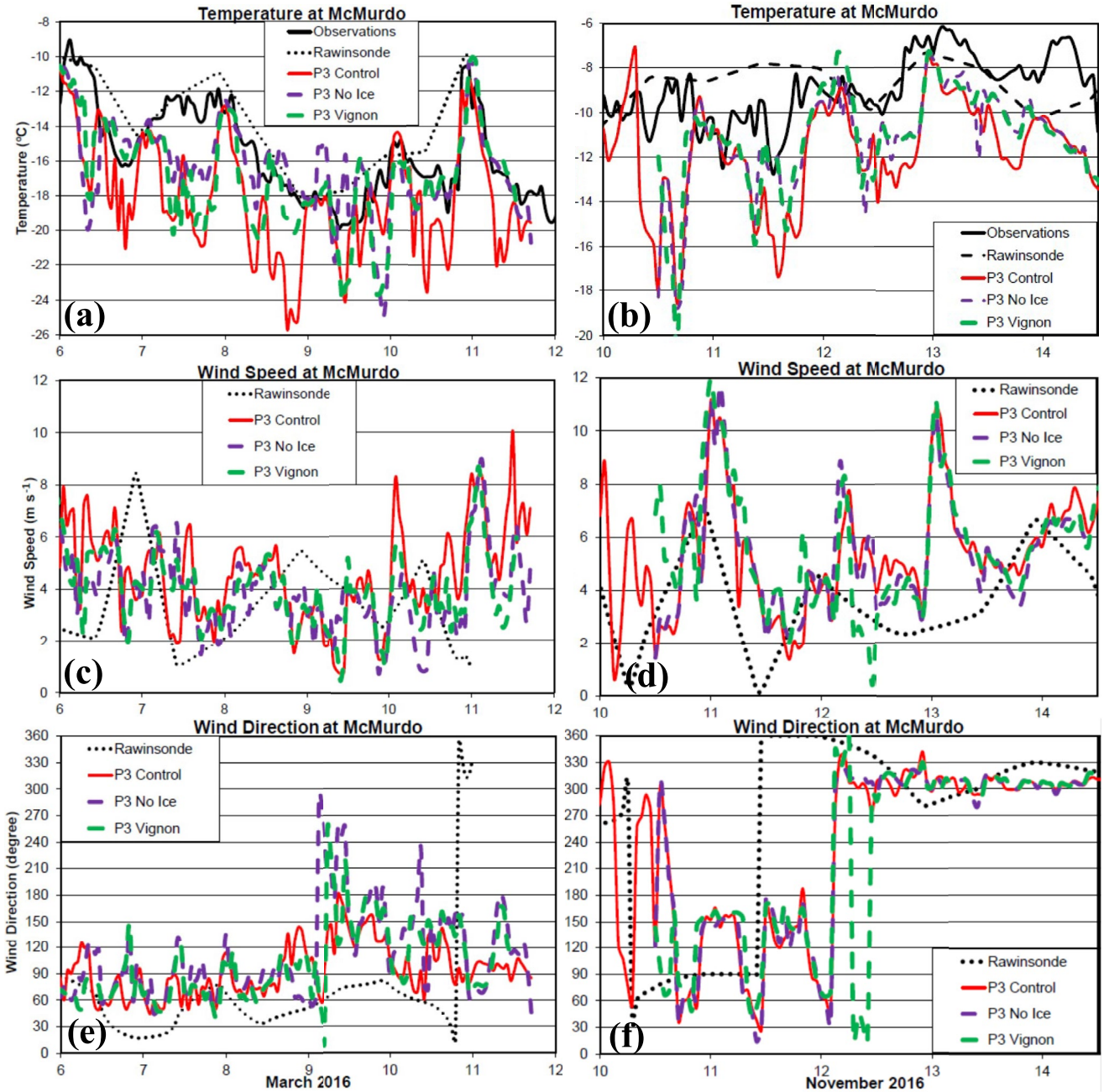

Figure 10. Time series of temperature (°C) for (a) March 2016 and (b) November, 10-m wind speed (m s^{-1}) for (c) March 2016 and (d) November 2016, and 10-m wind direction for (e) March 2016 and (f) November 2016. Near-surface observations are shown by solid black curves, 10-m rawinsonde observations are shown by dashed black curves, and model results are shown by color curves. The control simulations are shown by solid red curves, while sensitivity tests are shown by dashed curves.

impact on the radiation is demonstrated by Figure 12. The longwave cloud forcing at the surface is noticeably greater in VignonM than ControlM. By increasing the liquid water, the clouds have more radiative impact.

The scatter plots in Figure 13 demonstrate the impacts of the sensitivity to the Vignon ice microphysics change. The plots show 6-hr averages of liquid water path and downwelling longwave radiation, with the observations as the abscissa and the model results for the ordinate. Both the March and November cases are included in Figure 13. Regression lines are shown for the Control and the Vignon cases. The 6-hr averaging reduces the noise due to high-frequency variability. The Control simulations greatly underrepresent the liquid water path, especially when

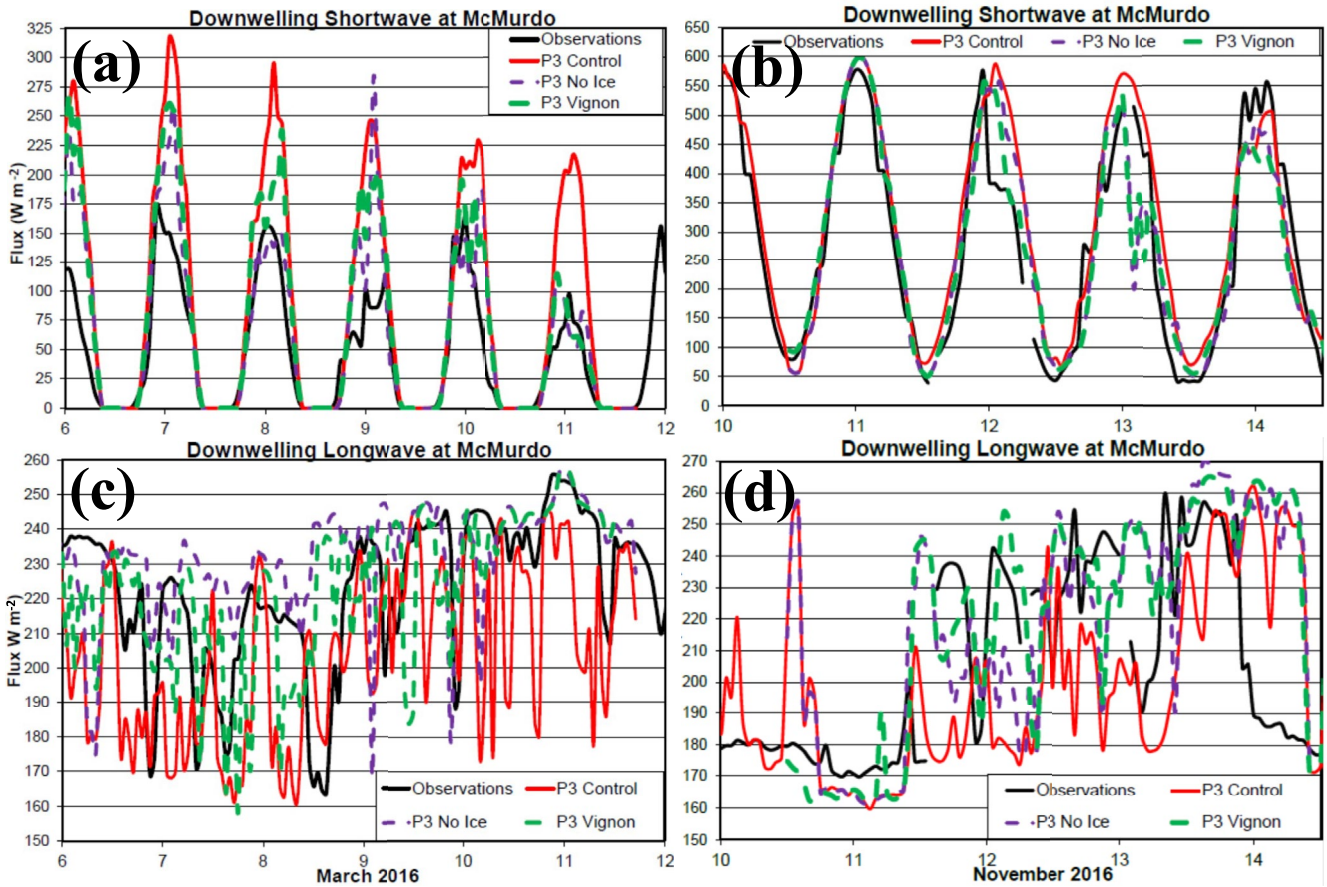

Figure 11. Time series of downwelling shortwave radiation (W m^{-2}) for (a) March 2016, and (b) November 2016, and downwelling longwave radiation (W m^{-2}) for (c) March 2016, and (d) November 2016. Observations are shown by solid black curves, while control simulations are shown by the solid red curves. The sensitivity simulations for the No Ice and Vignon cases are shown by the dashed purple and green curves, respectively.

the observed values are large (Figure 13a). Thus, its regression line has a slope of only 0.044. For the Vignon simulations, the liquid water path tends to be less than observed values, however, it is much greater than the Control values. Thus, the Vignon regression line is 0.686 as it better represents high liquid water path cases. The impact is seen in the longwave radiation where the incident flux at the surface is larger on the average for the Vignon cases for both low value cases and high value cases (Figure 13b). Interestingly, the average difference is actually larger for observed low value cases, in which clouds are thin and the average difference is about 20 W m^{-2} more than for high observed value cases, which should be associated with increased cloud optical depth. Accordingly, the regression lines have a slope of 0.317 for the Control cases and 0.228 for Vignon cases.

An interesting question about the changes to the microphysics is whether the impact results from increasing the frequency of clouds or by changing the optical thickness of clouds. We address this with the bar graphs in Figure 14 for the March case. Figure 14a demonstrates the frequency of "cloudy" cases from hourly values. Observed clouds are counted when the total cloud cover retrieved from remote sensing was 80% or greater. For Figure 14b,

Table 2
Cloud and Radiation Statistics for 12:00 UTC 1 February to 12:00 UTC 31 March 2016

Case	Cloud fraction	Liquid cloud fraction	Liquid water path (g m^{-2})	Ice water path (g m^{-2})	Shortwave at surface (W m^{-2})	Longwave at surface (W m^{-2})
Observations	0.72	0.35	12.6 (25)	28.6	154.6 (4)	208.3 (15)
FebMar Control	0.78	0.17	2.5	42.1	160.8	200.6
FebMar Vignon	0.77 (0.07)	0.43 (0.06)	23.3 (3)	25.8 (11)	133.1 (24)	201.3 (5)

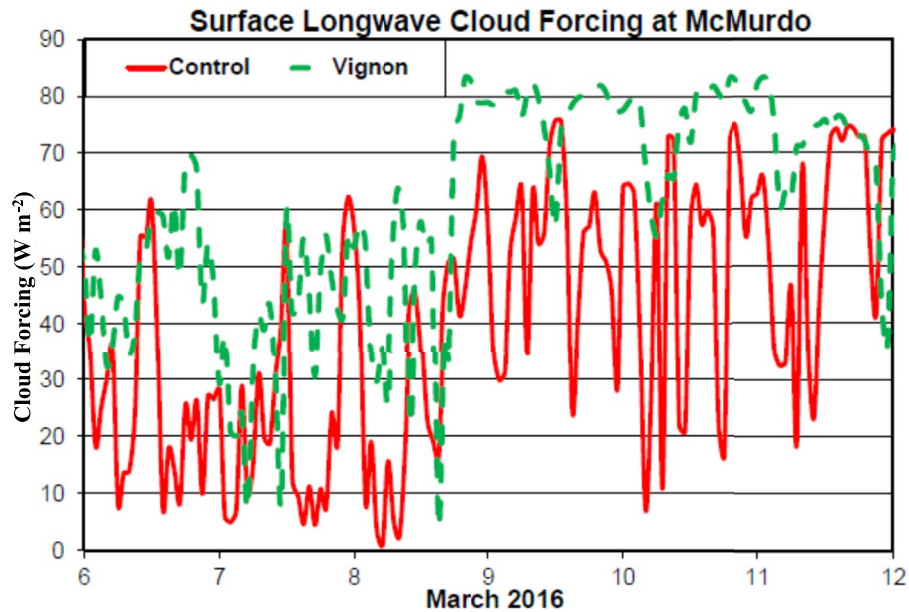

Figure 12. Time series of longwave cloud forcing (W m^{-2}) at the surface for ControlM (red) and VignonM (green).

"clear" observed cases have a retrieved value below 20%. Some observed cases fall in-between 20% and 80%. The procedure for detecting clouds is different for modeling results. We identify model clouds as present when the total hydrometeor mixing ratio exceeds 10^{-6} at any model level above surface and below 8,000 m AGL. To define low clouds, we use a common definition for the upper height, which is set at 2,000 m AGL (e.g., Hines & Bromwich, 2017). For liquid clouds, the hydrometeors must be liquid cloud or rain.

Figure 14a shows that by these methods more cloud cases are counted for the simulations than for the observations during the March case. In most cases, when clouds are present low clouds are also present (Figure 14c). For both the observations and model results, cases are classified as clear about 20% as frequent as cloudy cases (Figure 14b). Liquid low cloud cases are not common in either the observations or ControlM. The 80% threshold may contribute to the low count of observed liquid clouds. Liquid low clouds are much more common for the sensitivity tests, as the changes enable more liquid hydrometeors in our simulations (Figure 14d).

Figure 15 shows the average downwelling shortwave and longwave radiation for cases shown in Figures 14a and 14b. Error bars for the observations show the average in the uncertainty for these. The uncertainty is greater for the longwave observations than for the shortwave observations (Figures 15a and 15c). Furthermore, we should consider how sampling issues may impact the means of the simulations. Therefore, the *t*-test is used to indicate the probable range of means from sampling issues. Hourly ControlM values are used to compute the standard deviation, which is then imput into a computation of *t*. Blue arrows to the left of the ControlM values in Figure 15 bound the range between $t = -2$ and $t = 2$. For 5 degrees of freedom for example, and random samples, 90% of sample means are expected between $t = -2$ and $t = 2$ if sampling error is the only cause of difference between means. This allows us to interpret the statistical confidence for the differences between the sensitivity tests and ControlM, as seen in Figure 15. Sensitivity test means that fall within the range are not reliably different than ControlM means. As the diurnal cycle increases variance of shortwave radiation, the range between arrows is large in Figures 15a and 15b. The sensitivity tests appear to have statistically significant results during cloudy cases for shortwave and longwave radiation in Figures 15a and 15c, respectively.

The average downwelling shortwave for the 113 cloudy hourly events for the observations is 49.5 W m^{-2} (Figure 15a). The flux is much higher for the cloudy hourly events in ControlM, 87.2 W m^{-2}, indicating a much smaller optical depth. The ice microphysics changes in the sensitivity tests result in smaller fluxes. The values are 55.8 and 61.9 W m^{-2} for No IceM and VignonM, respectively. For downwelling longwave radiation, the two sensitivity tests appear to be statistically different than ControlM in Figure 15c. The microphysics changes increase the longwave radiation to values closer to the observed value 226.7 W m^{-2} for cloudy cases (Figure 15c).

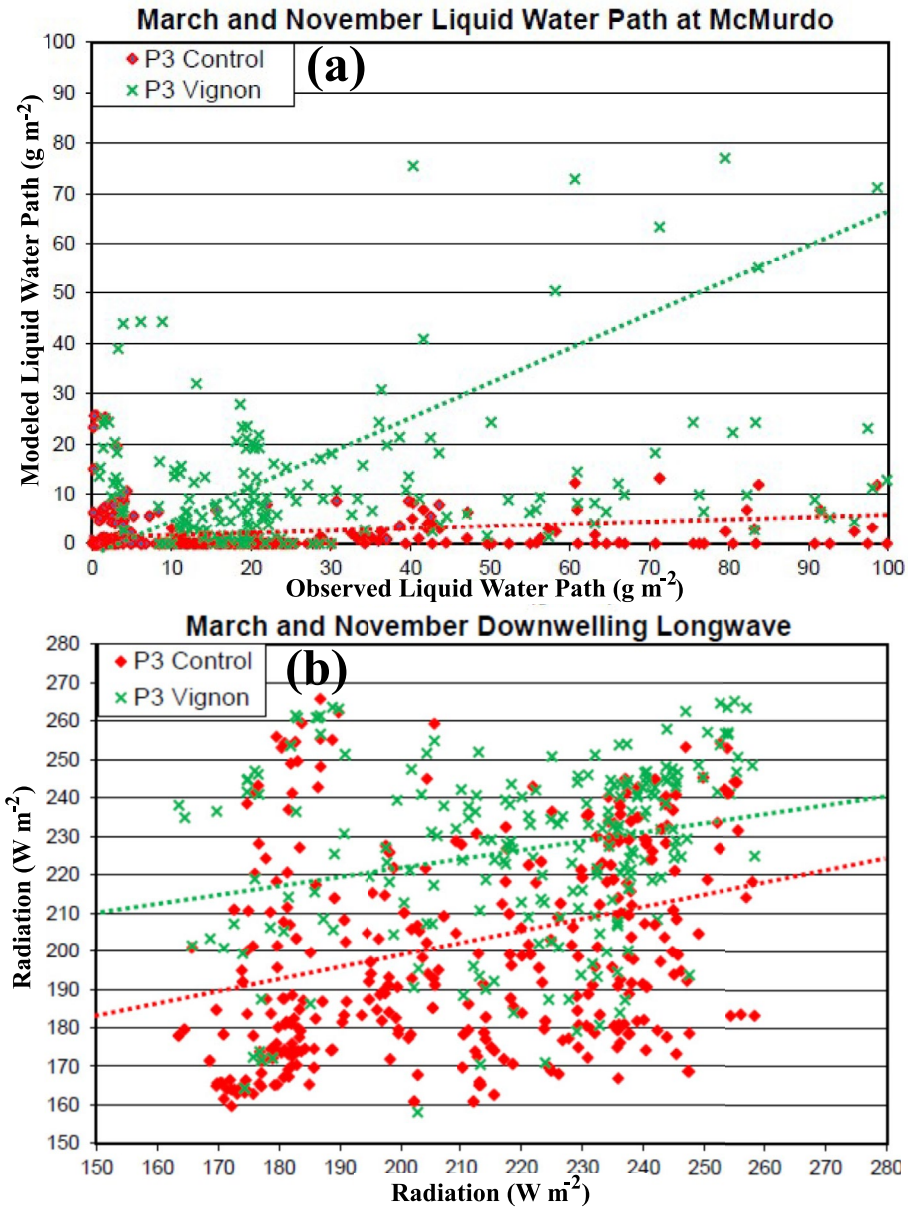

Figure 13. Scatter plots of (a) liquid water path (g m^{-2}) and (b) downwelling longwave radiation (W m^{-2}) for the combined March and November cases studies. The control simulations are shown by red diamonds and the Vignon simulations are shown by green crosses. The red (green) dotted curves show the regression line for the controls (VignonM and VignonN).

For clear-sky cases, the simulated radiant fluxes are sometimes larger and sometimes smaller than the observed values (Figures 15b and 15d). Overall, Figure 15 shows that the ice physics adjustments are increasing the cloud optical depth and impacting the radiative fluxes.

5. Summary and Conclusions

Supercooled liquid is common in the clouds near coastal Antarctica and occasionally occurs at temperatures below −30°C. However, given that the saturation vapor pressure with respect to ice is less than that with respect to liquid at subfreezing temperatures, the ice physics in most regional and global numerical models will typically glaciate out liquid clouds in cases well below freezing. This presents a challenge for the simulation of highly supercooled clouds that were observed at McMurdo, Antarctica during the 2015–2017 AWARE project (e.g.,

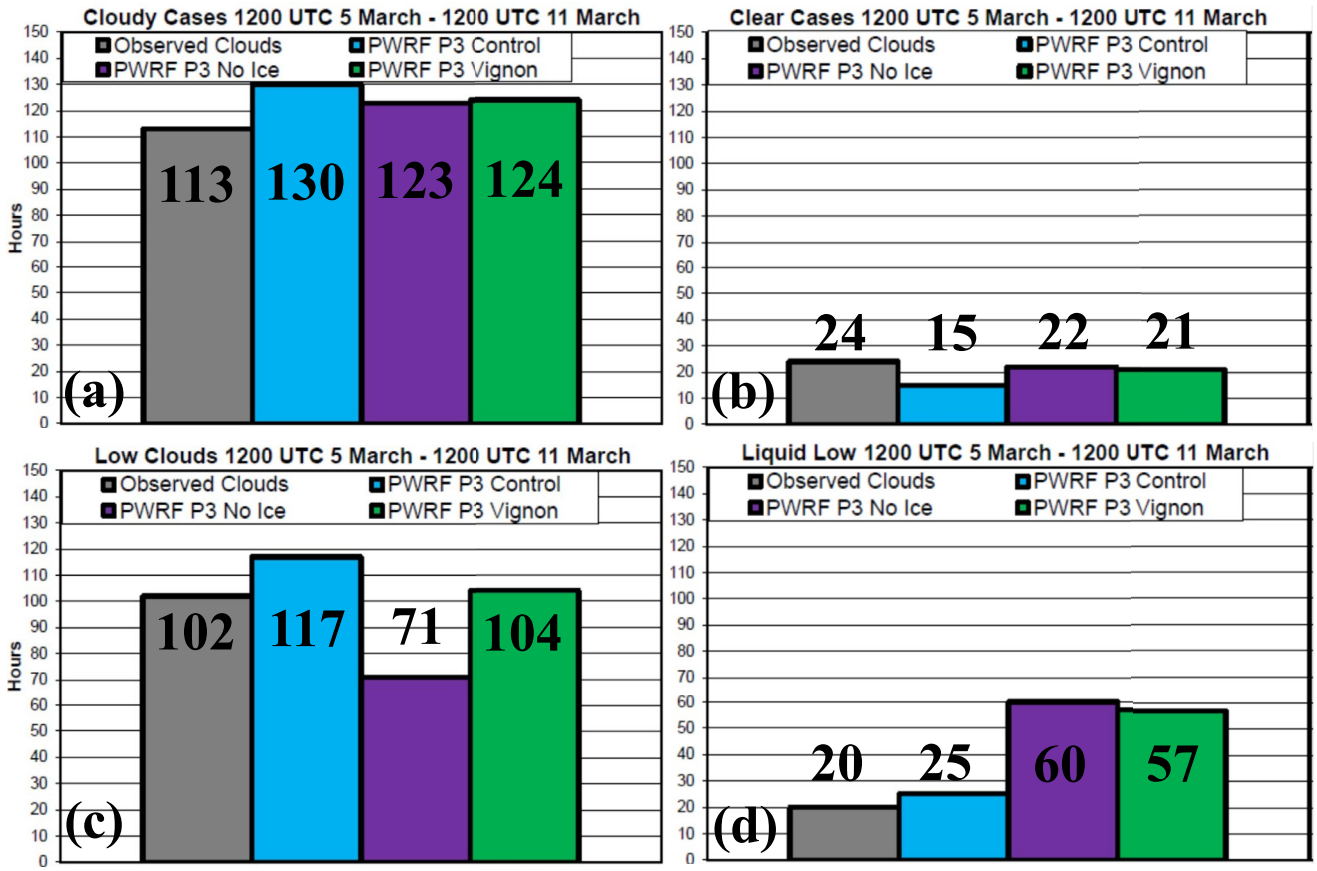

Figure 14. Number of hourly cases during 12:00 UTC 5 March to 12:00 UTC 11 March 2016. Gray shading shows observations, blue shading shows ControlM, purple shading shows No IceM, and green shading VignonM. (a) Cloud cover greater than 80%, (b) cloud cover less than 20%, (c) low cloud cover greater than 80%, and (d) liquid low cloud cover greater than 80%.

Silber, Fridlind, et al., 2019). We focus on such highly supercooled events during 5–11 March 2016 and 10–14 November 2016. Simulations with the advanced two-moment P3 microphysics scheme were conducted with version 4.1.1 of Polar WRF for these two events. Two-month simulations of February and March 2016 were also conducted for sampling over a variety of cloud ice and cloud liquid cases. These were compared to in-situ and remote sensing observations at McMurdo.

A good representation of the atmospheric moisture is required to represent the Antarctic clouds, however, our simulations are driven by the ERA5 reanalysis that has a regional dry bias that limits cloud development (e.g., Silber, Verlinde, Wang, et al., 2019). Fortunately, data assimilation to twice daily rawinsondes at McMurdo, Antarctic, and local AWS observations increases the atmospheric moisture content, and realistic values of precipitable water vapor are achieved. The result was much greater and more realistic hydrometeor amounts in our simulations. Mesoscale data assimilation may be an essential tool for cloud modeling studies in the future as it can help to overcome synoptic and mesoscale errors for the settings in which clouds develop.

The standard formulation of the P3 scheme produced too much ice condensate and too little liquid condensate at McMurdo. Sensitivity simulations for the ice microphysics reduced the amount of cloud ice. One sensitivity test intentionally removed much of the ice production for temperatures greater than −40°C. The other test was based upon the ice nucleation parameterization of Vignon et al. (2021) replacing the nucleation parameterization implemented in a standard microphysics scheme. Vignon et al. (2021) implemented the change for Southern Ocean simulations. In our two cold McMurdo cases, the ice physics change decrease cloud ice and increase the supercooled liquid toward more realistic amounts. The sensitivity tests also produce a representation of a liquid cloud layer near cloud top that is often observed in Antarctic coastal clouds. Ultimately, these physics changes increase the downwelling longwave radiation and decrease the downwelling shortwave radiation, and generally improve

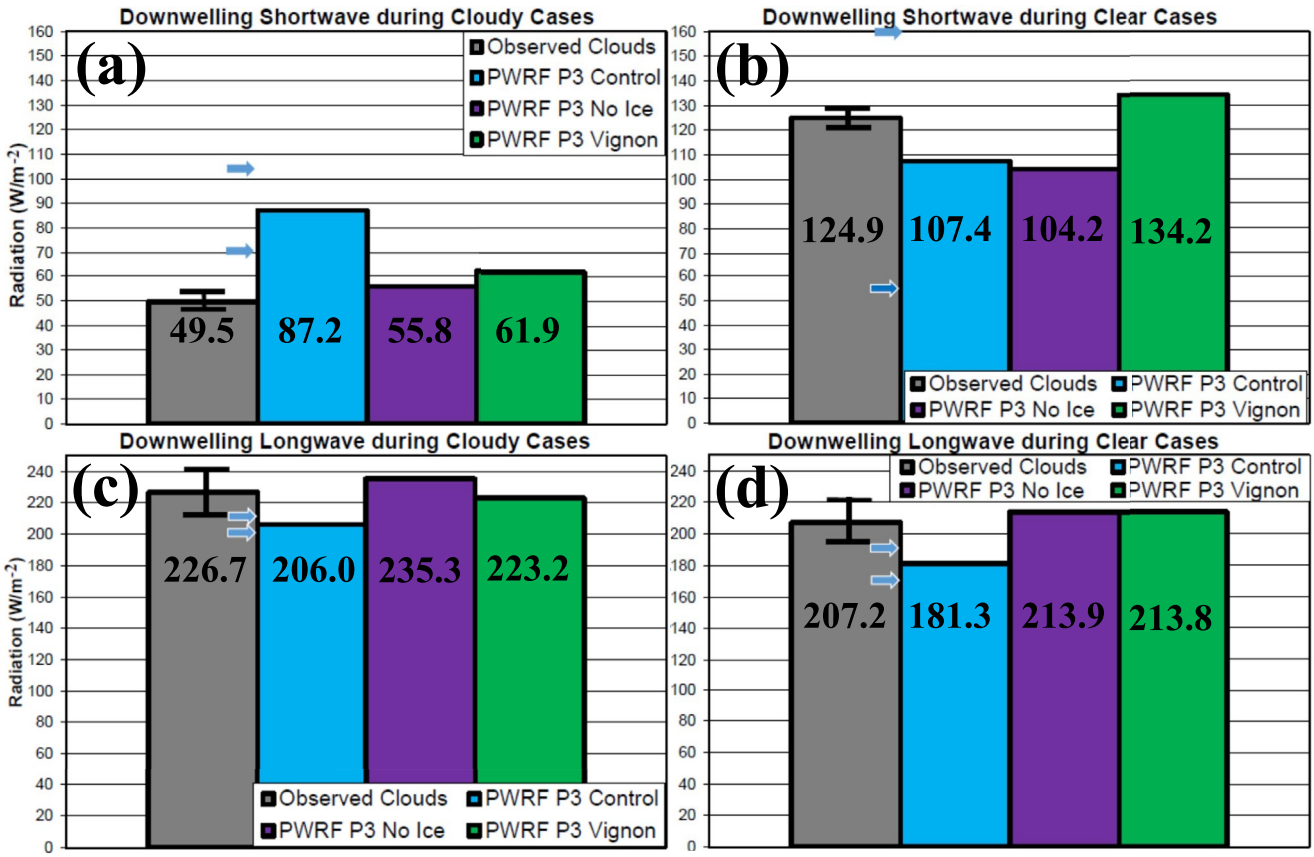

Figure 15. Incident surface radiation (W m^{-2}) for cloudy and clear cases during 12:00 UTC 5 March to 12:00 UTC 11 March 2016. Gray shading shows observations, blue shading shows ControlM, purple shading shows No IceM, and green shading shows VignonM. (a) Shortwave for cloudy cases, (b) shortwave for clear cases, (c) longwave for cloudy cases, and (d) longwave for clear cases. Error bars show the average of the uncertainty in the radiation observations. To indicate the statistical confidence of model sample means blue arrows show the range between $t = -2$ and $t = 2$ based upon the t-test applied to hourly values for ControlM.

the simulation results, including the representation of near-surface temperature. Furthermore, the 2-month simulation over February and March 2016 over a variety of liquid and ice cloud events at McMurdo shows that the Vignon et al. (2021) microphysics increases the liquid water path and liquid cloud fraction, while the unadjusted physics shows large deficits in these quantities. Therefore, the improvements extend over a broader range of synoptic conditions than the frigid supercooled events. Lower tropospheric wind speed and wind direction, however, are not necessarily improved by these changes. Getting both the correct amount of liquid water and ice in the clouds, however, remains a challenge for mesoscale simulations as increasing the liquid water can produce less than observed cloud ice. The Polar WRF simulations with the Vignon setting appear to produce the best balance between cloud liquid and cloud ice. Polar modelers should consider a number of factors when selecting model settings for their applications. These can include whether pristine conditions are present, or if secondary ice production is likely to occur.

In summary, accurate representation of INP concentrations appears to be critical for simulation of Antarctic clouds (see also Silber et al., 2021). Models such as the Community Atmosphere Model version 5 (CAM5) are already implementing prognostic cloud-aerosol physics (Xie et al., 2017). CAM5, however, simulates less than observed liquid water amounts over the Southern Ocean (e.g., D'Alessandro et al., 2019). The newer CAM6 has enhancements to cloud ice nucleation and simulates increased supercooled liquid (Gettelman et al., 2020). Yip et al. (2021) found that in contrast to the CAM5 results, CAM6 frequently overstimulates liquid water at McMurdo. While this may appear to be a contrarian result, it may emphasize the need for improved modeling of cases with enhanced ice particle amounts. Some recent studies emphasize that models may need enhanced secondary ice production (SIP) from the HM process and additional processes active at lower temperature (Fu et al., 2019; Sotiropoulou et al., 2021; Young et al., 2019). We encourage modeling work with both SIP processes

and predicted INP. Concentrations of INP can vary by several orders of magnitude in both time and space. Microphysics schemes that account for INP variations will provide a more general treatment, rather than case specific or regionally specific specifications.

Conflict of Interest

The authors declare no conflicts of interest relevant to this study.

Data Availability Statement

All the observations from the AWARE field campaign can be downloaded from the ARM Data Discovery website (http://www.archive.arm.gov/discovery/). These include soundings (Coulter et al., 1994), LIDAR (Eloranta et al., 2011), microwave radiometer (Gaustad & Riihimaki, 1996), and KAZR radar (Johnson et al., 2011, 2021). HSRL data can be obtained from the University of Wisconsin-Madison HSRL Lidar Group (http://lidar.ssec.wisc.edu). ERA5 reanalysis data are accessible via the Copernicus Climate Change Service (C3S) Climate Data Store (CDS; https://cds.climate.copernicus.eu). AMPS data (Powers et al., 2012) can be downloaded from the Ohio State University Polar Meteorology Group (http://polarmet.osu.edu/AMPS/). AWS observations are available from the University of Wisconsin's Antarctic AWS Program (Lazzara et al., 2012).

Acknowledgments
This research is supported by the DOE grant DE-SC0017981 and NSF Office of Polar Programs grant PLR-1443443. Numerical simulations were performed at the Ohio Supercomputer Center, which is supported by the State of Ohio. The authors thank Matthew Lazarra for assisting with Antarctic data. I. Silber was supported by DOE grants DE-SC0017981 and DE-SC0018046. This is Contribution 1606 of the Byrd Polar & Climate Research Center.

References

Barlage, M., Chen, F., Tewari, M., Ikeda, K., Gochis, D., Dudhia, D., et al. (2010). Noah land model modifications to improve snowpack prediction in the Colorado Rocky Mountains. *Journal of Geophysical Research: Atmospheres*, *115*, D22101. https://doi.org/10.1029/2009JD013470

Bigg, E. K. (1953). The supercooling of water. *Proceedings of the Physical Society. Section B*, *66*(8), 688–694. https://doi.org/10.1088/0370-1301/66/8/309

Bigg, E. K. (1973). Ice nucleus concentrations in remote areas. *Journal of the Atmospheric Sciences*, *30*, 1153–1157. https://doi.org/10.1175/1520-0469(1973)030<1153:incira>2.0.co;2

Bodas-Salcedo, A., Williams, K. D., Ringer, M. A., Beau, I., Cole, J. N. S., Dufresne, J.-L., et al. (2014). Origins of the solar radiation biases over the Southern Ocean in CFMIP2 models. *Journal of Climate*, *27*, 41–56. https://doi.org/10.1175/JCLI-D-13-00169.1

Bozkurt, D., Bromwich, D. H., Carrasco, J., Hines, K. M., Maureira, J. C., & Rondanelli, R. (2020). Recent near-surface temperature trends in the Antarctic Peninsula from observed, reanalysis and regional climate model data. *Advances in Atmospheric Sciences*, *37*, 477–493. https://doi.org/10.1007/s00376-020-9183-x

Bozkurt, D., Bromwich, D. H., Carrasco, J., & Rondanelli, R. (2021). Temperature and precipitation projections for the Antarctic Peninsula over the next two decades: Contrasting global and regional climate model simulations. *Climate Dynamics*, *56*, 3853–3874. https://doi.org/10.1007/s00382-021-05667-2

Bromwich, D. H., Hines, K. M., & Bai, L.-S. (2009). Development and testing of Polar Weather Research and Forecasting model: 2. Arctic Ocean. *Journal of Geophysical Research: Atmospheres*, *114*, D08122. https://doi.org/10.1029/2008JD010300

Bromwich, D. H., Nicolas, J. P., Hines, K. M., Kay, J. E., Key, E., Lazzara, M. A., et al. (2012). Tropospheric clouds in Antarctica. *Reviews of Geophysics*, *50*, RG1004. https://doi.org/10.1029/2011RG000363

Bromwich, D. H., Nicolas, J. P., Monaghan, A. J., Lazzara, M. A., Keller, L. M., Weidner, G. A., & Wilson, A. B. (2013). Corrigendum: Central West Antarctica among the most rapidly warming regions on Earth. *Nature Geoscience*, *6*(2), 139–145. https://doi.org/10.1038/ngeo1671

Bromwich, D. H., Otieno, F. O., Hines, K., Manning, K., & Shilo, E. (2013). Comprehensive evaluation of polar weather research and forecasting performance in the Antarctic. *Journal of Geophysical Research: Atmospheres*, *118*, 274–292. https://doi.org/10.1029/2012JD018139

Bromwich, D. H., Werner, K., Casati, B., Powers, J. G., Gorodetskaya, I. V., Massonnet, F., et al. (2020). The Year of Polar Prediction in the Southern Hemisphere (YOPP-SH). *Bulletin of the American Meteorological Society*, *101*, E1653–E1676. https://doi.org/10.1175/BAMS-D-19-0255.1

Bromwich, D. H., Wilson, A., Bai, L., Liu, Z., Barlage, M., Shih, C.-F., et al. (2018). The Arctic system reanalysis version 2. *Bulletin of the American Meteorological Society*, *99*(4), 805–828. https://doi.org/10.1175/BAMS-D-16-0215.1

Clough, S. A., Shephard, M. W., Mlawer, E. J., Delamere, J. S., Iacono, M. J., Cady-Pereira, K., et al. (2005). Atmospheric radiative transfer modeling: A summary of the AER codes. *Journal of Quantitive Spectroscopy and Radiative Transfer*, *91*(2), 233–244. https://doi.org/10.1016/j.jqsrt.2004.05.058

Cooper, W. A. (1986). Ice initiation in natural clouds. *Meteorological Monographs*, *21*, 29–32. https://doi.org/10.1007/978-1-935704-17-1_4

Coulter, R., Kyrouac, J., & Holdridge, D. (1994). *ARM: Balloon-borne sounding system (BBSS): Vaisala-processed winds, press., temp, and RH*. Oak Ridge National Laboratory. https://doi.org/10.5439/1021460

D'Alessandro, J. J., Diao, M., Wu, C., Liu, X., Jensen, J. B., & Stephens, B. B. (2019). Cloud phase and relative humidity distributions over the Southern Ocean in austral summer based on in situ observations and CAM5 simulations. *Journal of Climate*, *32*(7), 2781–2805. https://doi.org/10.1175/JCLI-D-18-0232.1

Deb, P., Orr, A., Bromwich, D. H., Nicolas, J. P., Turner, J., & Hosking, J. S. (2018). Summer drivers of atmospheric variability affecting ice shelf thinning in the Amundsen Sea Embayment, West Antarctica. *Geophysical Research Letters*, *45*(9), 4124–4133. https://doi.org/10.1029/2018GL077092

Deb, P., Orr, A., Hosking, J. S., Phillips, T., Turner, J., Bannister, D., et al. (2016). An assessment of the Polar Weather Research and Forecasting (WRF) model representation of near-surface meteorological variables over West Antarctica. *Journal of Geophysical Research: Atmospheres*, *121*(4), 1532–1548. https://doi.org/10.1002/2015JD024037

Eloranta, E. E. (2005). High spectral resolution lidar. In C. Weitkamp (Eds.), *Lidar*. Springer Series in Optical Sciences (Vol. 102, pp. 143–163). Springer. https://doi.org/10.1007/0-387-25101-4_5

Eloranta, E. E., Michelsen, H., Bambha, R. G., Ermold, B., & Goldsmith, J. (2011). *ARM: High spectral resolution lidar*. Oak Ridge National Laboratory. https://doi.org/10.5439/1025200

Field, P. R., Lawson, R. P., Brown, P. R. A., Lloyd, G., Westbrook, C., Moisseev, D., et al. (2017). Secondary ice production: Current state of the science and recommendations for the future. *Meteorological Monographs*, *58*(1), 7.1–7.20. https://doi.org/10.1175/AMSMONOGRAPHS-D-16-0014.1

Fletcher, N. H. (1962). The physics of rain clouds. *Quarterly Journal of the Royal Meteorological Society*, *88*(378), 559–559. https://doi.org/10.1002/qj.49708837821

Fu, S., Den, X., Shupe, M. D., & Huiwen, X. (2019). A modelling study of the continuous ice formation in an autumnal Arctic mixed-phase cloud case. *Atmospheric Research*, *228*(1), 77–85. https://doi.org/10.1016/j.atmosres.2019.05.021

Gaustad, K., & Riihimaki, L. (1996). *ARM: Microwave Radiometer Retrievals (MWRRET) of cloud liquid water and precipitable water vapor*. Atmospheric Radiation Measurement Archive, Oak Ridge National Laboratory. https://doi.org/10.5439/1285691

Gettelman, A., Bardeen, C. G., McCluskey, C. S., & Järvinen, E. (2020). Simulating observations of Southern Ocean clouds and implications for climate. *Journal of Geophysical Research: Atmospheres*, *125*. https://doi.org/10.1029/2020jd032619

Grosvenor, D. P., Choularton, T. W., Lachlan-Cope, T., Gallagher, M., Crosier, J., Bower, K. N., et al. (2012). In-situ aircraft observations of ice concentrations within clouds over the Antarctic Peninsula and Larsen Ice Shelf. *Atmospheric Chemistry and Physics*, *12*, 11275–11294. https://doi.org/10.5194/acp-12-11275-2012

Hersbach, H., Bell, B., Berrisford, P., Hirahara, S., Horányi, A., Muñoz-Sabater, J., et al. (2020). The ERA5 global reanalysis. *Quarterly Journal of the Royal Meteorological Society*, *146*, 1999–2049. https://doi.org/10.1002/qj.3803

Hines, K. M., & Bromwich, D. H. (2008). Development and testing of Polar Weather Research and Forecasting (WRF) model. Part I: Greenland Ice Sheet meteorology. *Monthly Weather Review*, *136*(6), 1971–1989. https://doi.org/10.1175/2007MWR2112.1

Hines, K. M., & Bromwich, D. H. (2017). Simulation of late summer Arctic clouds during ASCOS with Polar WRF. *Monthly Weather Review*, *145*, 521–541. https://doi.org/10.1175/MWR-D-16-0079.1

Hines, K. M., Bromwich, D. H., Bai, L., Bitz, C. M., Powers, J. G., & Manning, K. W. (2015). Sea ice enhancements to Polar WRF. *Monthly Weather Review*, *143*(6), 2363–2385. https://doi.org/10.1175/MWR-D-14-00344.1

Hines, K. M., Bromwich, D. H., Wang, S.-H., Silber, I., Verlinde, J., & Lubin, D. (2019). Microphysics of summer clouds in central West Antarctica simulated by Polar WRF and AMPS. *Atmospheric Chemistry and Physics*, *19*(19), 12431–12454. https://doi.org/10.5194/acp-19-12431-2019

Hogan, A. W. (1986). Aerosol exchange in the remote troposphere. *Tellus*, *38*(3–4), 197–213. https://doi.org/10.3402/tellusb.v38i3-4.15129

Hogan, R. J., Mittermaier, M. P., & Illingworth, A. J. (2006). The retrieval of ice water content from radar reflectivity factor and temperature and its use in evaluating a mesoscale model. *Journal of Applied Meteorology and Climatology*, *45*, 301–317. https://doi.org/10.1175/JAM2340.1

Hyder, P., Edwards, J. M., Allan, R. P., Hewitt, H. T., Bracegirdle, T. J., Gregory, J. M., et al. (2018). Critical Southern Ocean climate model biases traced to atmospheric model cloud errors. *Nature Communications*, *9*, 3625. https://doi.org/10.1038/s41467-018-05634-2

Intrieri, J. M., Fairall, C. W., Shupe, M. D., Persson, P. O. G., Andreas, E. L., Guest, P. S., & Moritz, R. E. (2002). An annual cycle of Arctic surface cloud forcing at SHEBA. *Journal of Geophysical Research: Oceans*, *107*, 8039. https://doi.org/10.1029/2000JC000439

Johnson, K., Toto, T., & Giangrande, S. (2021). *KAZRCORGE-c0*. Atmospheric Radiation Measurement Archive, Oak Ridge National Laboratory. https://doi.org/10.5439/1389054

Johnson, K., Toto, T., & Jensen, M. (2011). *ARM: Ka ARM Zenith Radar (KAZR): Moderate sensitivity mode corrected*. Oak Ridge National Laboratory. https://doi.org/10.5439/1350634

Jousse, A., Hall, A., Sun, F., & Teixeira, J. (2016). Causes of WRF surface energy fluxes biases in a stratocumulus region. *Climate Dynamics*, *46*, 571–584. https://doi.org/10.1007/s00382-015-2599-9

King, J. C., Gadian, A., Kirchgaessner, A., Kuipers Munneke, P., Lachlan-Cope, T. A., Orr, A., et al. (2015). Validation of the summertime surface energy budget of Larsen C Ice Shelf (Antarctica) as represented in three high-resolution atmospheric models. *Journal of Geophysical Research: Atmospheres*, *120*, 1335–1347. https://doi.org/10.1002/2014JD022604

Korolev, A., McFarquhar, G., Field, P. R., & Franklin, C. (2017). Mixed-phase clouds: Progress and challenges. *Meteorological Monographs*, *58*. 5.1–5.50. https://doi.org/10.1175/amsmonographs-d-17-0001.1

Lachlan-Cope, T., Beddows, D. C. S., Brough, N., Jones, A. E., Harrison, R. M., Lupi, A., et al. (2020). On the annual variability of Antarctic aerosol size distributions at Halley Research Station. *Atmospheric Chemistry and Physics*, *20*, 4461–4476. https://doi.org/10.5194/acp-20-4461-2020

Lachlan-Cope, T., Listowski, C., & O'Shea, S. (2016). The microphysics of clouds over the Antarctic Peninsula – Part 1: Observations. *Atmospheric Chemistry and Physics*, *16*(24), 15609–15617. https://doi.org/10.5194/acp-16-15605-2016

Lazzara, M. A., Weidner, G. A., Keller, L. M., Thom, J. E., & Cassano, J. J. (2012). Antarctic Automatic Weather Station Program: 30 years of polar observations. *Bulletin of the American Meteorological Society*, *93*(10), 1519–1537. https://doi.org/10.1175/BAMS-D-11-00015.1

Listowski, C., Delanoë, C. J., Kirchgaessner, A., Lachlan-Cope, T., & King, J. (2019). Antarctic clouds, supercooled liquid water and mixed phase, investigated with DARDAR: Geographical and seasonal variations. *Atmospheric Chemistry and Physics*, *19*(10), 6771–6808. https://doi.org/10.5194/acp-19-6771-2019

Listowski, C., & Lachlan-Cope, T. (2017). The microphysics of clouds over the Antarctic Peninsula. Part 2: Modelling aspects within Polar WRF. *Atmospheric Chemistry and Physics*, *17*(17), 10195–10221. https://doi.org/10.5194/acp-17-10195-2017

Liu, J., Dedrick, J., Russell, L. M., Senum, G. I., Uin, J., Kuang, C., et al. (2018). High summertime aerosol organic functional group concentrations from marine and seabird sources from Ross Island, Antarctica during AWARE. *Atmospheric Chemistry and Physics*, *18*(12), 8571–8587. https://doi.org/10.5194/acp-18-8571-2018

Lubin, D., Zhang, D., Silber, I., Scott, R. C., Kalogeras, P., Battaglia, A., et al. (2020). AWARE: The atmospheric radiation measurement (ARM) west Antarctic radiation experiment. *Bulletin of the American Meteorological Society*, *101*, E1069–E1091. https://doi.org/10.1175/BAMS-D-18-0278.1

McCluskey, C. S., Hill, T. C. J., Humphries, R. S., Rauker, A. M., Moreau, S., Strutton, P. G., et al. (2018). Observations of ice nucleating particles over southern ocean waters. *Geophysical Research Letters*, *45*, 11989–11997. https://doi.org/10.1029/2018GL079981

McCoy, D. T., Hartmann, D. L., Zelinka, M. D., Ceppi, P., & Grosvenor, D. P. (2015). Mixed-phase cloud physics and Southern Ocean cloud feedback in climate models. *Journal of Geophysical Research: Atmospheres*, *120*, 9539–9554. https://doi.org/10.1002/2015JD023603

McFarquhar, G. M., Bretherton, C., Marchand, R., Protat, A., DeMott, P. J., Alexander, S. P., et al. (2021). Observations of clouds, aerosols, precipitation, and surface radiation over the Southern Ocean: An overview of CAPRICORN, MARCUS, MICRE, and SOCRATES. *Bulletin of the American Meteorological Society*, *102*(4), E894–E928. https://doi.org/10.1175/BAMS-D-20-0132

Meyers, M. J., Demott, P. J., & Cotton, W. R. (1992). New primary ice-nucleation parameterizations in an explicit cloud model. *Journal of Applied Meteorology and Climatology*, *31*(7), 708–721. https://doi.org/10.1175/1520-0450(1992)031<0708:NPINPI>2.0.CO;2

Miao, J., Kunzi, K., Heygster, G., Lachlan-Cope, T. A., & Turner, J. (2001). Atmospheric water vapor over Antarctica derived from Special Sensor Microwave/Temperature 2 data. *Journal of Geophysical Research: Atmospheres*, *106*, 10187–10203. https://doi.org/10.1029/2000JD900811

Morrison, H., Curry, J. A., Khvorostyanov, V. I., & Zuidema, P. (2005). A new double-moment microphysics scheme for application in cloud and climate models. Part I: Description. *Journal of the Atmospheric Sciences*, *62*(6), 1665–1693. https://doi.org/10.1175/JAS3446.1

Morrison, H., de Boer, G., Feingold, G., Harrington, J., Shupe, M. D., & Sulia, K. (2012). Resilience of persistent Arctic mixed-phase clouds. *Nature Geoscience*, *5*(1), 11–17. https://doi.org/10.1038/ngeo1332

Morrison, H., & Milbrandt, J. A. (2015). Parameterization of cloud microphysics based on the prediction of bulk ice particle properties. Part I: Scheme description and idealized tests. *Journal of Atmospheric Sciences*, *72*(1), 287–311. https://doi.org/10.1175/JAS-D-14-0065.1

Nakanishi, M., & Niino, H. (2006). An improved Mellor–Yamada level-3 model: Its numerical stability and application to a regional prediction of advection fog. *Boundary-Layer Meteorology*, *119*, 397–407. https://doi.org/10.1007/s10546-005-9030-8

Nicolas, J. P., Scott, R. C., Cadeddu, M. P., Bromwich, D. H., Verlinde, J., Lubin, D., et al. (2017). January 2016 extensive summer melt in West Antarctica favoured by strong El Nino. *Nature Communications*, *8*, 15799. https://doi.org/10.1038/ncomms15799

O'Shea, S. J., Choularton, T. W., Flynn, M., Bower, K. N., Gallagher, M., Crosier, J., et al. (2017). In situ measurements of cloud microphysics and aerosol over coastal Antarctica during the MAC campaign. *Atmospheric Chemistry and Physics*, *17*(21), 13049–13070. https://doi.org/10.5194/acp-17-13049-2017

Pon, K. (2015). *The representation of low cloud in the Antarctic Mesoscale Prediction System* (MS thesis, p. 80). Atmospheric Sciences Program, Department of Geography, The Ohio State University. https://library.ohio-state.edu

Powers, J. G., Manning, K. W., Bromwich, D. H., Cassano, J. J., & Cayette, A. M. (2012). A decade of Antarctic science support through AMPS. *Bulletin of the American Meteorological Society*, *93*, 1699–1712. https://doi.org/10.1175/BAMS-D-11-00186.1

Rignot, E. (2008). Changes in West Antarctic ice stream dynamics observed with ALOS PALSAR data. *Geophysical Research Letters*, *35*, L12505. https://doi.org/10.1029/2008GL033365

Scott, R. C., & Lubin, D. (2016). Unique manifestations of mixed-phase cloud microphysics over Ross Island and the Ross Ice Shelf, Antarctica. *Geophysical Research Letters*, *43*, 2936–2945. https://doi.org/10.1002/2013JD021132

Scott, R. C., Lubin, D., Vogelmann, A. M., & Kato, S. (2017). West Antarctic Ice Sheet cloud cover and surface radiation budget from NASA A-Train satellites. *Journal of Climate*, *30*, 6151–6170. https://doi.org/10.1175/JCLI-D-16-0644.1

Scott, R. C., Nicolas, J. P., Bromwich, D. H., Norris, J. R., & Lubin, D. (2019). Meteorological drivers and large-scale climate forcing of West Antarctic surface melt. *Journal of Climate*, *32*, 665–684. https://doi.org/10.1175/JCLI-D-18-0233.1

Seefeldt, M. W., & Cassano, J. J. (2012). A description of the Ross Ice Shelf air stream (RAS) through the use of self-organizing maps (SOM). *Journal of Geophysical Research: Atmospheres*, *117*. https://doi.org/10.1029/2011JD016857

Shupe, M. D., & Intrieri, J. M. (2004). Cloud radiative forcing of the Arctic surface: The influence of cloud properties, surface albedo, and solar zenith angle. *Journal of Climate*, *17*, 616–628. https://doi.org/10.1175/1520-0442(2004)017<0616:crfota>2.0.co;2

Shupe, M. D., Tjernström, M., & Persson, P. O. G. (2015). Challenge of Arctic clouds and their implications for surface radiation [in "State of the Climate in 2014"]. *Bulletin of the American Meteorological Society*, *96*(7), S130–S141. https://doi.org/10.1175/2015BAMSStateoftheClimate.1

Shupe, M. D., Uttal, T., Matrosov, S. Y., & Frisch, A. S. (2001). Cloud water contents and hydrometeor sizes during the FIRE Arctic Clouds Experiment. *Journal of Geophysical Research: Atmospheres*, *106*, 15015–15028. https://doi.org/10.1029/2000jd900476

Silber, I., Fridlind, A. M., Verlinde, J., Ackerman, A. S., Cesana, G. V., & Knopf, D. A. (2021). The prevalence of precipitation from polar supercooled clouds. *Atmospheric Chemistry and Physics*, *21*, 3949–3971. https://doi.org/10.5194/acp-21-3949-2021

Silber, I., Fridlind, A. M., Verlinde, J., Ackerman, A. S., Chen, Y.-S., Bromwich, D. H., et al. (2019). Persistent supercooled drizzle at temperatures below −25°C observed at McMurdo Station, Antarctica. *Journal of Geophysical Research: Atmospheres*, *124*, 10878–10895. https://doi.org/10.1029/2019JD030882

Silber, I., Verlinde, J., Cadeddu, M., Flynn, C. J., Vogelmann, A. M., & Eloranta, E. W. (2019). Antarctic cloud macrophysical, thermodynamic phase, and atmospheric inversion coupling properties at McMurdo Station—Part II: Radiative impact during different synoptic regimes. *Journal of Geophysical Research: Atmospheres*, *124*, 1697–1719. https://doi.org/10.1029/2018JD029471

Silber, I., Verlinde, J., Eloranta, E. W., & Cadeddu, M. (2018). Antarctic cloud macrophysical, thermodynamic phase, and atmospheric inversion coupling properties at McMurdo Station: I. Principal data processing and climatology. *Journal of Geophysical Research: Atmospheres*, *123*, 6099–6121. https://doi.org/10.1029/2018JD028279

Silber, I., Verlinde, J., Wang, S.-H., Bromwich, D. H., Fridlind, A. M., Cadeddu, M., et al. (2019). Cloud influence on ERA5 and AMPS surface downwelling longwave radiation biases in West Antarctica. *Journal of Climate*, *32*(22), 7935–7949. https://doi.org/10.1175/JCLI-D-19-0149.1

Skamarock, W. C., Klemp, J. B., Dudhia, J., Gill, D. O., Barker, D. M., Duda, M. G., et al. (2008). *A description of the Advanced Research WRF version 3*. *NCAR Technical note NCAR/TN-475+STR* (p. 125). http://dx.doi.org/10.5065/D68S4MVH

Sotiropoulou, G., Sullivan, S., Savre, J., Lloyd, G., Lachlan-Cope, T., Ekman, A. M. L., & Nenes, A. (2020). The impact of secondary ice production on Arctic stratocumulus. *Atmospheric Chemistry and Physics*, *20*, 1301–1316. https://doi.org/10.5194/acp-20-1301-2020

Sotiropoulou, G., Vignon, E., Young, G., Morrison, H., O'Shea, S. J., Lachlan-Cope, T., et al. (2021). Secondary ice production in summer clouds over the Antarctic coast: An underappreciated process in atmospheric models. *Atmospheric Chemistry and Physics*, *21*(2), 755–771. https://doi.org/10.5194/acp-21-755-2021

Steig, E. J., Schneider, D. P., Rutherford, S. D., Mann, M. E., Comiso, J. C., & Schindell, D. T. (2009). Warming of the Antarctic ice-sheet surface since the 1957 International Geophysical Year. *Nature*, *457*, 459–462. https://doi.org/10.1038/nature07669

Steinhoff, D. F., Bromwich, D. H., Lambertson, M., Knuth, S. L., & Lazzara, M. A. (2008). A dynamical investigation of the May 2004 McMurdo Antarctica severe wind event using AMPS. *Monthly Weather Review*, *136*(1), 7–26. https://doi.org/10.1175/2007mwr1999.1

Tetzner, D., Thomas, E., & Allen, C. (2019). A validation of ERA5 Reanalysis data in the southern Antarctic Peninsula—Ellsworth Land region, and its implications for ice core studies. *Geosciences*, *9*, 289. https://doi.org/10.3390/geosciences9070289

Vergara-Temprado, J., Miltenberger, A. K., Furtado, K., Grosvenor, D. P., Shipway, B. J., Hill, A. A., et al. (2018). Strong control of Southern Ocean cloud reflectivity by ice-nucleating particles. *Proceedings of the National Academy of Sciences*, *115*, 2687–2692. https://doi.org/10.1073/pnas.1721627115

Vignon, E., Alexander, P. S., DeMott, P. J., Sotiropoulou, G., Gerber, F., Hill, T. C. J., et al. (2021). Measured ice nucleating particle concentrations improve the simulation of mid-level mixed-phase clouds over the high-latitude Southern Ocean. *Journal of Geophysical Research Atmospheres*, *126*. https://doi.org/10.1029/2020jd033490

Wille, J. D., Bromwich, D. H., Cassano, J. J., Nigro, M. A., Mateling, M. E., Lazzara, M. A. & Wang, S. H. (2017). Evaluation of the AMPS boundary-layer simulations on the Ross Ice Shelf, Antarctica, with unmanned aircraft observations. *Journal of Applied Meteorology and Climatology*, *56*(8), 2239–2258. https://doi.org/10.1175/JAMC-D-16-0339.1

Xie, X., Zhang, H., Liu, X., Peng, Y., & Liu, Y. (2017). Sensitivity study of cloud parameterizations with relative dispersion in CAM5.1: Impacts on aerosol indirect effects. *Atmospheric Chemistry and Physics*, *17*(9), 5877–5892. https://doi.org/10.5194/acp-17-5877-2017

Yip, J., Diao, M., Barone, T., Silber, I., & Gettelman, A. (2021). Evaluation of the CAM6 climate model using cloud observations at McMurdo Station, Antarctica. *Journal of Geophysical Research: Atmospheres*, *126*, e2021JD034653. https://doi.org/10.1029/2021JD034653

Young, G., Lachlan-Cope, T., O'Shea, S. J., Dearden, C., Listowski, C., Bower, K. N., et al. (2019). Radiative effects of secondary ice enhancement in coastal Antarctic clouds. *Geophysical Research Letters*, *46*, 2312–2321. https://doi.org/10.1029/2018GL080551

Reference From the Supporting Information

Monaghan, A. J., Bromwich, D. H., Powers, J. G., & Manning, K. W. (2005). The climate of the McMurdo, Antarctic region as represented by one year of forecasts from the Antarctic Mesoscale Prediction System. *Journal of Climate*, *18*(8), 1174–1189. https://doi.org/10.1175/JCLI3336.1